ELECTRICAL STEEL FABRICATED BY BINDER JET PRINTING

By

Hoi Ho Hawke Suen

A DISSERTATION

Submitted to
Michigan State University
in partial fulfillment of the requirements
for the degree of

Mechanical Engineering – Doctor of Philosophy

2023

ABSTRACT

Binder Jet Printing has been a promising additive manufacturing (AM) technique since it was first patented 30 years ago. The nature of its densification process is similar to powder metallurgy. Compared to other methods such as powder bed fusion and direct energy deposition, it provides many unique benefits, minimal residual stress, cost-efficient scaling up, higher powder reusability, etc. However, for most metals, the final density obtainable from the binder jet printing is low compared to other AM methods, making the technique only suitable for few materials or limited in applications such as prototyping. This study implemented liquid phase sintering and a linear packing model to achieve high-density electrical steel starting from pure elemental powders as well as pre-alloyed powders. Boron and Silicon were used as additives to form a eutectic composition with Iron to achieve liquid phase sintering. The elemental powder approach investigated the effect of Boron and Silicon on mechanical and magnetic properties with the ANOVA technique. The alloyed powder approach with Boron and Silicon as additives achieved the final density of 7.39 g/cc (98.4% of the theoretical density 7.51 g/cc), 8489.75 in maximum permeability, 0.053 Ws/kg for hysteresis loss at 1.5T, and a total loss of 34.39 W/kg for the frequency at 400Hz and 0.5T. These values can be compared to Cramer et al. [1] which achieved the final density of 7.31 g/cc (97.3% of the theoretical density of 7.51 g/cc), 10500 in maximum permeability, and 62.85 W/kg at 400Hz and 0.5T. With the processing parameters implemented, the stator with internal cooling channels was made with a unique joining technique. It shows that binder jet printing is a promising technique for fabricating free-form electrical steels without the preferred orientation offered by sheet lamination but with improved strength and density compared to soft magnetic composites.

This dissertation is dedicated to my parents

ACKNOWLEDGEMENTS

This research is supported by the Department of Navy, Office of Naval Research, under ONR Award Number N00014-18-1-2514.

First, I thank my parents for their love and support throughout my life. Thank you both for believing in me and giving me the strength to chase my dreams.

I want to thank my mentor and advisor, Dr. Patrick Kwon, for his support and guidance throughout my research and confidence in me.

I would also like to thank Dr. Shanelle Foster, Dr. Haseung Chung & Dr. Himanshu Sahasrabudhe for serving as my thesis committee members and for the valuable comments and support on my research. I want to thank Dr. Junghoon Yeom, Dr. Carl Boehlert, Dr. Yang Guo, and Dr. Alejandro Diaz for their guidance and support at MSU (Michigan State University), Dr. Craig Gunn for giving suggestions on the dissertation writing.

I thank my fellow lab members and friends: Guangchao (Jack) Song, Bo Li, Yuheng Wang, Jianxin Zhao, Hao Li, Hoa X Nguyen, Tyler Bauder, Thang Q Pham, Bibek Poudel, Zhiyuan (Carson) Qu, Siqi (Jack) Zhao, Xiaolu (Amberly) Huang, Yaozhong (Ragnar) Zhang, Tanzilur Rahman, Tareq Sarower, Matt Meier, Geeta Kumari, Jazib Islam, Juan Sandoval, Jisheng Chen, Ryan Khawarizmi, Mohsan Uddin Ahmad, Aaron Oneil, Beytullah Aydogan, Tho Trung Do, Dinh Nguyen, for helping me in experiments, helpful discussions, and all the fun we had.

To all my friends and family, I thank you for the support, understanding, and accompanying me through my best and worst times. I cannot list all the names here, but you are always on my mind.

Lastly, I would like to thank my girlfriend, Yuening Xu, for her love, support, and being my best friend. I will always cherish every single day with you.

TABLE OF CONTENTS

CHAPTER 1 INTRODUCTION

1.1 Background

Since the first patented device [2] in the early 1970s, 3D printing (or a more commonly used term in the industry is Additive Manufacturing (AM)) has been continuously developed and exhibits the potential to fabricate complex parts in a more efficient, economical way. In the beginning, the industry considered AM to be only suitable for prototypes. The limitations from repeatability, precision, and material choice, constrained the application of the technology. Hence, the term to describe additive manufacturing was "rapid prototyping." Through the progress from the last 40 years, the limitations of AM improved step by step, more accurate devices, repeatable results, and different methods of fabricating samples. Currently, there are seven process categories in AM according to the current ISO/ASTM standards [3], shown as Figure 1.1: binder jetting (BJT), directed energy deposition (DED), material extrusion (MEX), material jetting (MJT), powder bed fusion (PBF), sheet lamination (SHL) and vat photopolymerization (VPP). In the following section, every category will be introduced briefly then will mainly focus on binder jetting (BJT).

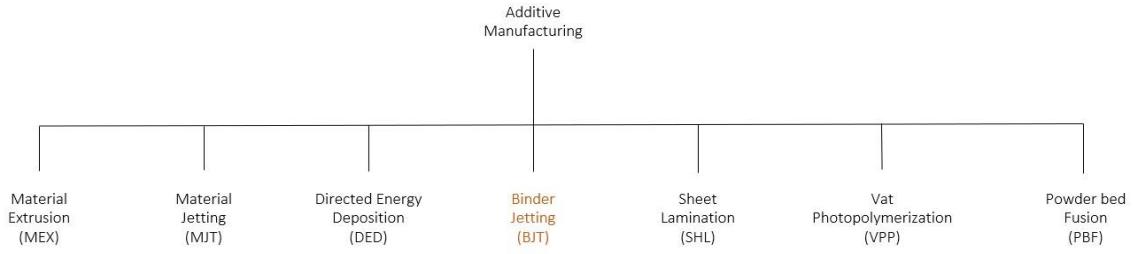

Figure 1.1 Tree of AM process categories, binder jetting is the main focus of this study

1.2 AM Processes

1.2.1 Material Extrusion (MEX)

In Material Extrusion (MEX), the material stock is dispensed selectively through a nozzle or orifice [3], Figure 1.2 is an illustration of the MEX process. The stock material must soften and push through a nozzle. The print head can move in the XY location to deposit the material in the desired

location in each layer. After the material is hardened, it will start a new layer on top of the previous layer as the build platform moves down to deposit the next layer. The process is repeated until the final part is completed. Currently, the material spool that the extruder can push through the nozzle, bond with the previous layer, and retain their shape after its hardening is typically used for MEX. Most of the materials are plastic. But, to print metal parts, the material stock usually is in the form of a composite of metal powder and a thermoplastic material. The volume ratio of the mixture contains 40-60% metal powder. After a part is completely printed, it is debinded and then sintered. Usually, printing parts with overhanging features needs supports underneath to prevent sagging.

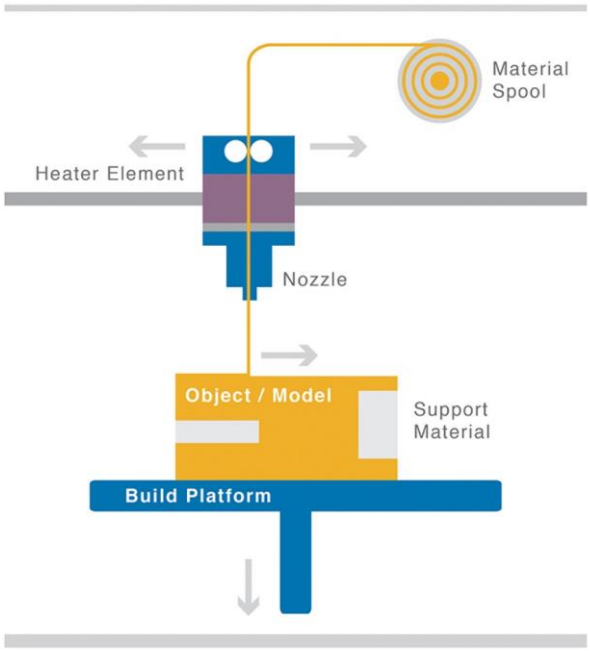

Figure 1.2 Material Extrusion process [4]

1.2.2 Vat Photopolymerization (VPP)

Vat photopolymerization (VPP), also known as stereolithography (SLA), is a process by which the material stock is liquid, which is selectively cured by light-activated polymerization, turning it into a solid [3]. It was considered the first industrial AM technology. Conventionally, the light beam draws or projects the 2D layer image to the layer. Once the layer is hardened, the build platform moves to allow the resin to fill the new layer and the process repeats until the 3D object is completed. A schematic of a metal based VPP process presented with our patent-pending process

called Scalable and Expeditious Additive Manufacturing (SEAM) is shown in Figure 1.3. The material choice for VPP is mainly photocurable polymer, either epoxy- or acrylate-based. For metal applications, metal powder is mixed with the photopolymer. The volume ratio for the mixture contains a similar metal to polymer ratio as MEX. The part is formed similarly to photocurable polymer, but after the built the printed piece must be debinded and then sintered into the final part. Ceramic parts are also possible with the VPP process.

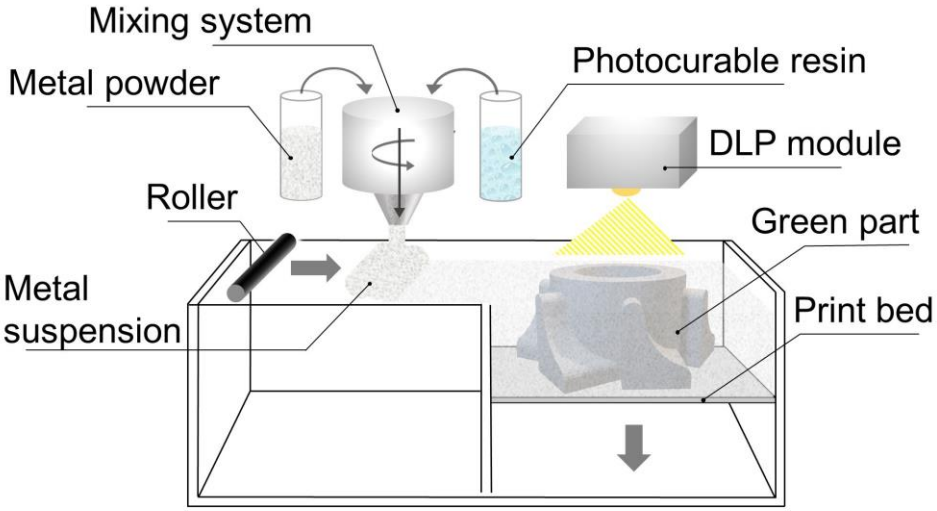

Figure 1.3 Schematic of a metal AM process SEAM [5]

1.2.3 Directed Energy Deposition (DED)

Directed Energy deposition (DED) is when the material stock is melted and fused by focused thermal energy while being deposited. The thermal energy can be any energy source (e.g., laser, electron beam, or plasma arc) [3]. The material stock (in a powder or wire form) is pushed through the nozzle then melted and deposited by the focused energy source, which is usually mounted near the nozzle of a multi-axis arm. After a layer is deposited and solidified, the subsequent layer deposits on top. The process is repeated until the final part is finished. Although the process is in a similar fashion to MEX, the energy consumption is in an order of magnitudes different. Figure 1.4 shows two schematic views of the DED printhead, with different material feeding methods. Depositing can also be done in multiple directions depending on the degree of freedom of the multi-axis arm.

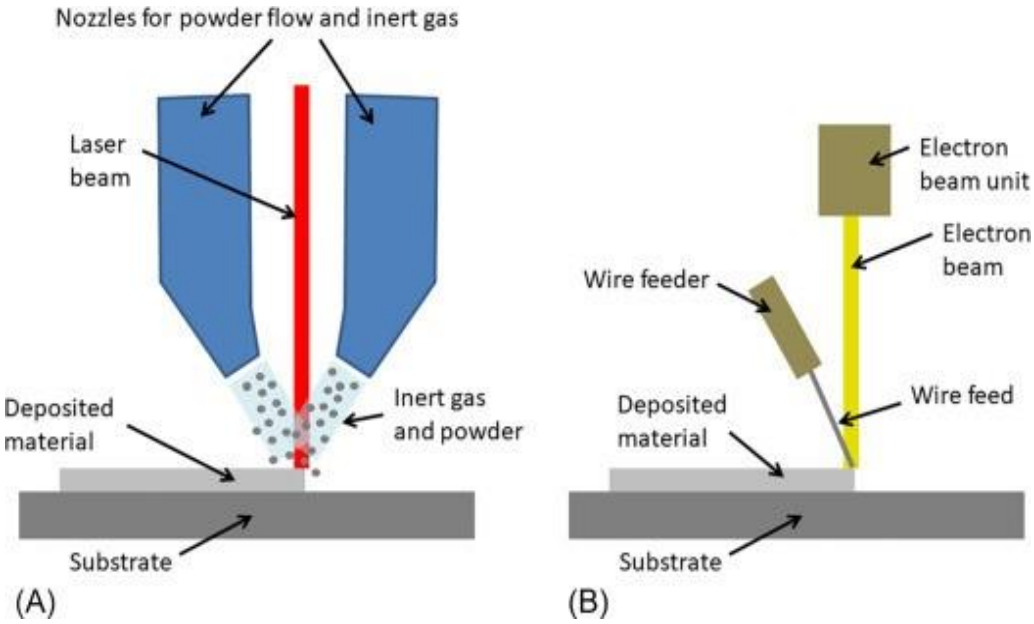

Figure 1.4 Schematic of a nozzle for DED [6] (A) powder feed (B) wire feed

1.2.4 Material Jetting (MJT)

Material Jetting (MJT) is a process in which the droplets and feedstock material are selectively deposited [3]. One can consider the process as a combination of 2D inkjet printing and VPP. The printhead shoots hundreds of tiny droplets of material stock and support material into the selected area. Then, the droplets are cured by either UV-light curing, cooling, or drying. After that, the build platform moves down for the next layer and the process is repeated until the whole part is completed. The final piece is finished by removing the part from the supports. Figure 1.5 illustrates the MJT printing method and an example of its capability. Given that the printed head and system are designed to dispense various materials, MJT is suitable to print objects made of a variety of materials. In addition to a base material to be printed, another necessary material for MJT is photocurable polymer or self-hardened resins. Currently, there are no extensive investigations into the use of MJT for processing metals. This presents a potentially appealing research focus, since functionally graded material has consistently drawn considerable interest via AM [7].

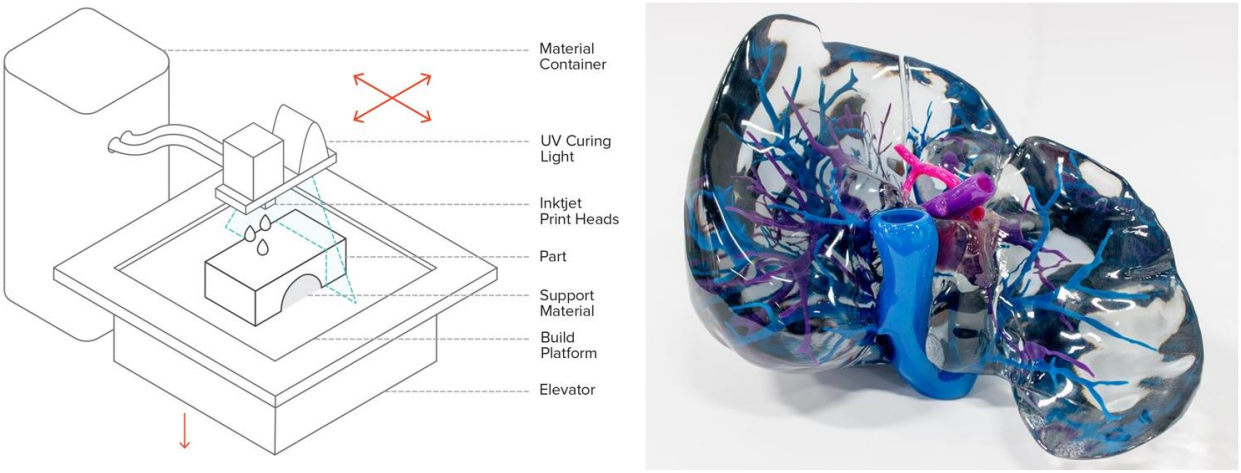

Figure 1.5 A demonstration of the components, method, and capability of MJT. Left: Various components of and MJT 3D printer [8] Right: A model made with the help of material jetting [9]

1.2.5 Sheet Lamination (SHL)

Sheet lamination is a process in which the sheets of material are bonded and then cut to form a part [3]. The 2D cross-section is cut out either before or after the lamination. The two main sheet lamination methods are ultrasonic additive manufacturing (UAM) and laminated object manufacturing (LOM). In UAM, the metal sheets are bonded with mechanical pressure and ultrasonic vibrations by disrupting the oxide layers of the materials by plastic deformation [10], and LOM uses an adhesive coating to bond sheets of material. UAM allows joining different metals to make "functionally graded materials" (FGM). For LOM, the most common materials are A4 paper and thin plastic sheets. Figure 1.6 is an example of a metal part made by UAM method.

Figure 1.6 UAM Mini Heat Exchanger and Dissimilar Metal Examples [11]

1.2.6 Powder Bed Fusion (PBF)

Powder Bed Fusion is a process where energy selectively fuses regions of the powder bed [3]. When the fusion occurs, the powder bed must be always in a vacuum or inert gas filled chamber. Depending on the technique, the thermal energy source is directed and fuses the powder in the selected region. After the powder solidifies, the build platform goes down a layer; then, a new layer of powder is deposited on the top of the previous layer. The procedure is repeated until the whole part is completed. Figure 1.7 is a schematic of the laser powder bed fusion (L-PBF) process. The most common thermal energy source for PBF is the laser. In such a case, the process can also be called selective laser melting (SLM). The powder bed usually stays in an inert gas environment. Another choice for energy source is an accelerated electron beam. In this case, the process is called electron beam melting (EBM). The material range for this category is broad. Plastic to ceramics and metals in granular formed can be processed. However, the process parameters need to be optimized precisely for specific materials to have consistent quality.

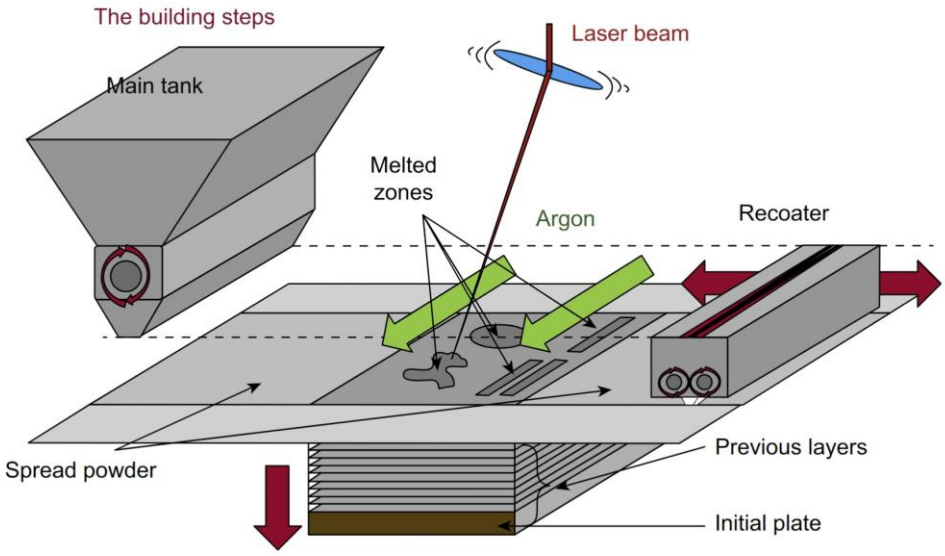

Figure 1.7 A Schematic illustration of the laser-based powder bed fusion process [12]

1.3 Binder Jetting (BJT)

Binder jetting is a process in which powder is temporarily bonded by depositing a liquid binding agent to selected regions [3]. Much like PBF, BJT also requires a powder bed to build the part, and every layer is recoated from the material stock after finishing the previous layer. As the liquid

binding agent is jetted, the binder agent will start to harden at least partially, so the shape and feature are intact during printing. The common term for the printed part is called the “green part.” The green part is then moved to a furnace and cured at a specific temperature depending on the binding agent used. The final densification condition varies depending on the processed material. Most of the material in a granular form can be processed by BJT, including metals, plastic, sand, and ceramic. For metal and ceramic, debinding and sintering steps are required to consolidate the part. The following section of this chapter will explain the processes of BJT by dividing it into two main phases: Part Printing and Post Processing. Figure 1.8 shows our printer used in this study.

Figure 1.8 A picture of the X1-Lab in MSU

1.3.1 Part Printing

The part printing process plays can vary among the printers. However, the basic principle is the same; the difference is mainly on how the printer executes the binder injection and powder layering. The BJT printer used in this study is an X1-Lab model manufactured by ExOne (Huntington, PA, USA). The printer contains two beds: a supply bed where the powder stock is stored and a building bed where the desired structure is printed. Once the powder stock is prepared, the required amount of powder is placed in the supply bed, and a metal base plate is placed in the build bed. The initial layer for a build is prepared as follows: the powder stock is pushed upward more than one layer of powders depending on the powder feed ratio[1], and the powder roller starts to spread the powder across the build bed. With the initial layer ready, a new layer of powder is spread across the build bed and the printhead with 127 nozzles deposits the binder liquid into the selected area. The amount of binder to be deposited is determined by the variable called saturation[2]. The selected area on each layer where the binder must be deposited is determined by the computer-aided design (CAD) file sectioned by the printer's control software. After depositing the binder on each layer, the build bed is heated up to about 90°C. This step is designed for drying the newly deposited binder by providing some strength to the green part, which ensures that the part does not collapse or deform inside the build bed throughout the printing process. After this precuring step, the build bed moves down one layer and the supply bed moves up a set layer depending on the powder feed ratio, then the roller starts the powder spreading process again. The process is repeated until the entire part is finished. A schematic of the binder jet is shown in Figure 1.9.

1.3.2 Post Processing

Post-processing usually requires multiple steps depending on the powder. For metal materials, the process can be divided into binder curing, binder burnout, and part sintering.

[1] The powder feed ratio is the ratio between the amount of powders being spread and the amount of powders needed, e.g. 2:1 powder feed ratio means that 2 layers worth of powder will be spread across the powder bed for one layer needed for printing.

[2] The saturation rate is the volume ratio between the voids among powders and binder liquid. 70% saturation rate means that: 70% of the interstitial space among the powders is occupied by the liquid binder.

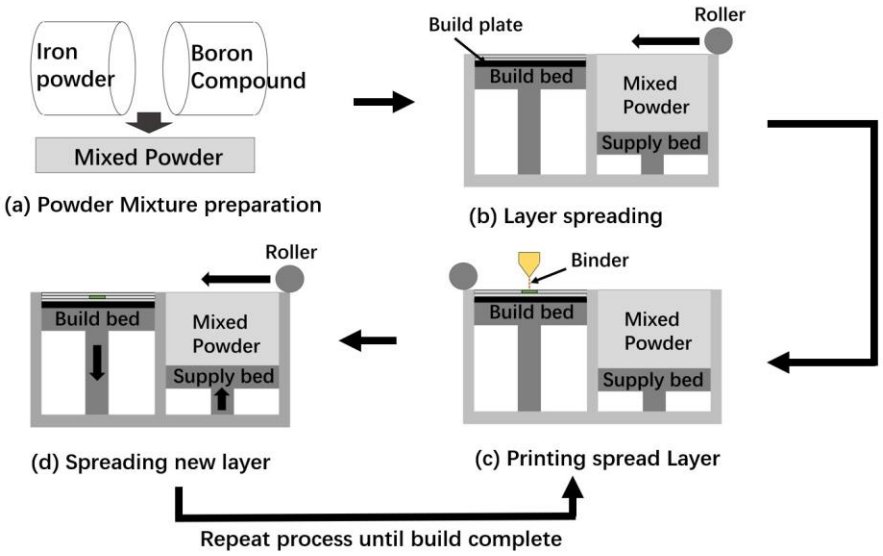

Figure 1.9 A schematic illustration of the printing process for X1-Lab

1.3.2.1 Binder Curing

After the part is printed, the printed (or green) part with the base plate is extracted from the build bed. Some of the loose powders can be brushed or blown off, which can be reused in future prints. Then the printed part is placed in an air furnace. The target temperature and the dwell time may vary depending on the binder liquid used for the printing process. The FluidFuse™ binder provided from ExOne (Huntington, PA, USA) requires the dwell time of at least 2 hours at 195°C for the binder to harden. For larger samples, a longer curing time is needed.

1.3.2.2 Binder Burnout

After the binder curing process for the printed part, binder burnout is recommended if the process does not compromise the integrity of the material. The binder phase contains about 0.5% of the part weight [13], which can be a significant source of undesirable carbon in the final part. If the material can be oxidized during the binder burnout procedure, an alternative way is needed to remove the carbon content. If there is no alternative way to remove the binder without compromising the material, one must consider the additional carbon residual in the final part during analysis.

1.3.2.3 Part Densification

After the binder curing and the optional burnout processes, the sample is ready for densification, also known as the sintering process. The part is placed in an environment-controlled furnace at high temperature. The temperature and environment of the furnace are dependent on the material. Usually, this is the final step in the process. Sometimes other post-processing (e.g., hot isostatic pressing (HIP), annealing) may be required to enhance the mechanical properties.

1.3.3 Advantages & Limitations

Metal additive manufacturing has some unique challenges as each metal may require different processing conditions. At the same time, each AM process, including the BJT process, has its own strengths and weaknesses.

1.3.3.1 Advantages

The first advantage is that the BJT process is more economical than most other metal additive manufacturing methods. For PBF, the powder bed is usually concealed in an envelope to maintain an inert or vacuum environment during the printing process, which is costly to maintain. If the build volume needs to scale up, the price of maintaining such an envelope will scale up proportionally. However, the BJT process takes place at room temperature and in an ambient air environment. In scaling up the print bed there is no need for scaling up an enclosed envelope for environment control, a larger furnace can be purchased according to the production size. The other factor of making BJT an economical process is the reusability of the powders due to the fact that the BJT process does not require a high temperature during printing. For example, SS316 can be reused up to 16 times according to [14].

The second advantage of the BJT process is its ability to produce parts with homogeneous material properties due to its distinct printing and densification approach. As the printing and densification stages occur independently, densification takes place uniformly across the entire printed part by heating the green part in an environment-controlled furnace. The DED and PBF processes melts and solidifies the material during printing, which leads to a heterogeneous microstructure. While it is not impossible for PBF and DED to fabricate microstructural homogenous parts, the post-processing requirements for doing so are significantly more complex compared to those for BJT.

The uniform temperature for sintering BJT parts also leads to the third advantage. The part has minimal residual stress compared to PBF and DED methods. Because the residual stress hardly builds up for BJT parts during the densification process. For PBF and DED methods, residual stress can build up quickly due to the nature of the printing process with rapid cooling and heating of the raw material [15, 16].

The fourth advantage is printing overhanging features without supporting structures. The powder bed can act as the support structure for the overhanging features during printing. Compared to PBF and DED, designing the support structure is essential for conducting heat from the melt pool for the PBF process or to prevent sagging for overhanging features for the DED process. An inadequate support structure can lead to sagging or swelling in the final part.

Figure 1.10 One of the furnaces used in this study. Carbon liner resistance furnace in MSU: MRF T-16X26-G-G-3000-VM-G

1.3.3.2 Limitations

The first limitation for BJT is that the final parts are prone to retain pores because of its densification method. Unlike PBF and DED where the material is melted during printing, the densification process for BJT is limited to mostly solid-state sintering. The remaining pores in the final part lead to poor mechanical properties, making the processed parts unsuitable for structural use. Figure 1.11 shows the microstructure difference between Ti-6Al-4V parts process by EBM and BJT, the porosity in the BJT processed samples are obvious. Although some post-processing such as hot isostatic pressing (HIP) can improve the density of the final part, it makes the whole process significantly more expensive. The second limitation is that the binder curing and burnout process could oxidize the part for some materials. If the printed part does not undergo binder burnout, the remaining binding agents will add carbon in the final part. The third issue is that the green parts are usually too weak to handle between the printer and the furnaces.

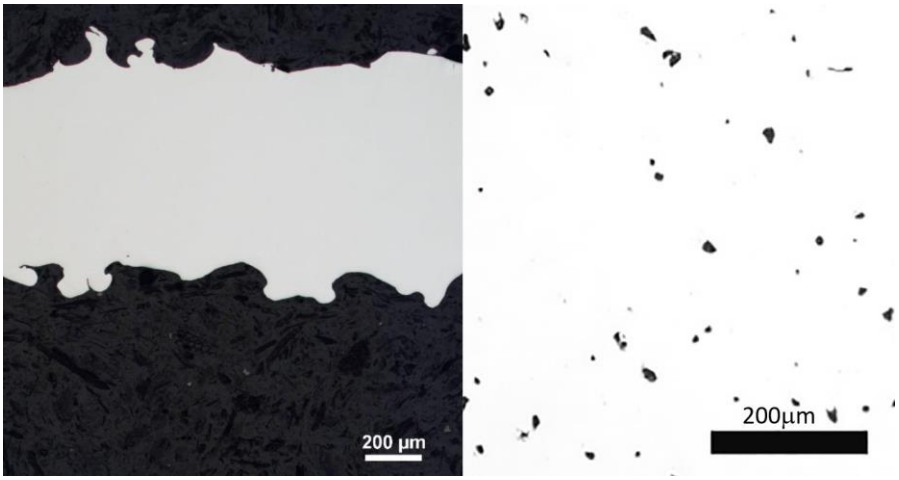

Figure 1.11 left: EBM produced Ti64 sample right: BJT sample sintered in 1420°C for 2hrs [17]

1.4 Research objectives

The BJT process offers many advantages, but it needs to be refined and optimized to resolve the forementioned limitations. The objective of this study is to focus on solving two limiting issues. The first one is to increase the density of the processed part to improve other properties such as strength and shape. The second one is to process electrical steel with BJT to achieve similar properties compared to conventional processing methods.

1.5 Proposed research

To accomplish these objectives, two methods are used to optimize the process: liquid phase sintering [18] and a linear packing model [19]. The following section will explain the details of the two methods.

1.5.1 Liquid Phase Sintering

Liquid phase sintering is defined as sintering involving both a liquid and particulate solid phase during some part of the thermal cycle [20]. This technique using clay and porcelain has been used in the ceramic industry for centuries. In modern manufacturing, liquid phase sintering has been studied and practiced in the powder metallurgy industry [18]. This sintering technique utilizes a liquid phase to accelerate the bonding among solid phases. The liquid phase can be induced by a few different methods. The first method is called infiltration, which introduces a material that has a significantly lower melting temperature compared to the printed material. During the densification process, the temperature is set at the melting point of the introduced material infiltrating the interstitial space among the particulate solid phase. However, the infiltration method requires a significant amount of additional low-melting material into the alloy [21], essentially making the final different from the intended material and limiting the application. The second method is simply setting the sintering temperature near the melting point and the material itself will partially melt and form a liquid phase. With this method, the final part has similar properties to the base alloy. However, this process makes the part difficult to keep a near net shape after the densification process, because the gravitational force will distort the part slightly as the whole part is being heated near the melting temperature. The third method utilizes the eutectic phase between at least two distinct materials. In practice, a small amount of additive was added into the powder stock and, during the sintering phase, the temperature is set to the eutectic temperature, which can ensure the liquid phase is formed locally where the additives are located (Figure 1.12), and the materials mostly remains in a solid state. This method allows adjusting the measure of liquid phase during the sintering process by controlling the amount of additives in the powder stock and ensures that the part would not deform extensively. This method will be the main focus of this study.

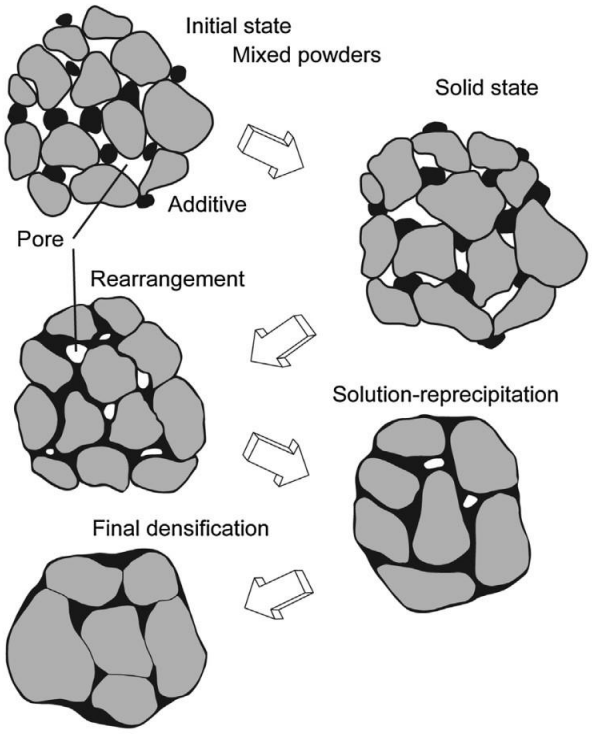

Figure 1.12 A schematic of the microstructure changes during liquid phase sintering [20]

1.5.2 Linear Packing Model

For BJT and PBF, the material stock usually comes in a spherical powder form for a better flowability [22]. The packing density is an essential property of a powder, which directly relates to the final part density. The better packed powder means less interstitial space among the powder, which benefits the densification process by reducing the extent of material migration needed.
Less interstitial space also affects the saturation rate. With the amount of binder fixed, the volume of the interstitial space is reduced, which can ultimately increase the green part strength [23]. The linear packing model utilizes a smaller-sized powder to fill in the interstitial space among the larger powders to increase the packing density of the mixture. In Figure 1.13, three typical packing scenarios are shown. For scenario A, the voids are mainly created by small powders since it is the dominate powder size in the mixture. This kind of packing will increase the total cost of the powder stock since finer powders (typically in the range of 0.1-10 μm) are usually more expensive than regular-sized ones (20-100 μm). Scenario B shows an insufficient number of small powders, leading to voids unfilled in the mixture. The ideal scenario is C, where smaller particles fill out

most of the interstitial space among the larger particles. Figure 1.14 shows the result of processing K418 alloy with BJT and it shows that the optimal mixing ratio produces the highest final density [19]. In some cases, better-packed powders also have a better print quality, since the addition of smaller powders in the mixture can increase friction of the powder stock, preventing sliding between layers as shown in Figure 1.15.

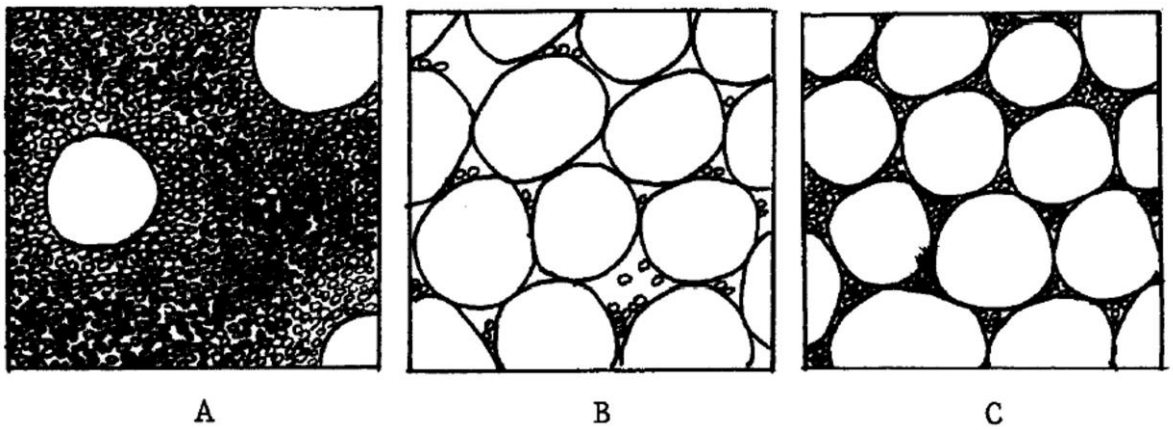

Figure 1.13 Typical packing arrangements of binary mixtures [19]. A) An Excessive amount of smaller powders B) An Insufficient amount of smaller powders C) An Optimal amount of powder ratio

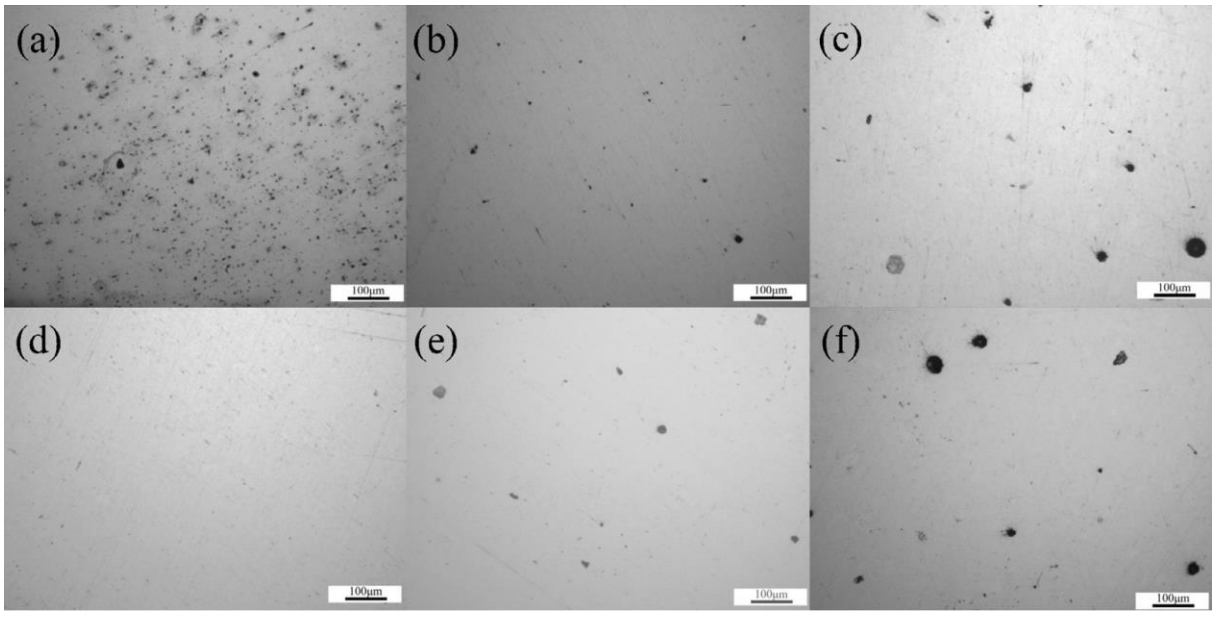

Figure 1.14 Micrographs of sintered material show the variation in pore size and volume due to varying volume fractions of coarse (100mm) to fine (10 mm) in sintered K418 alloy [24] (a) 0:1 (b) 1:1 (c) 2:1 (d) 4:1 (e) 6:1 (f) 1:0

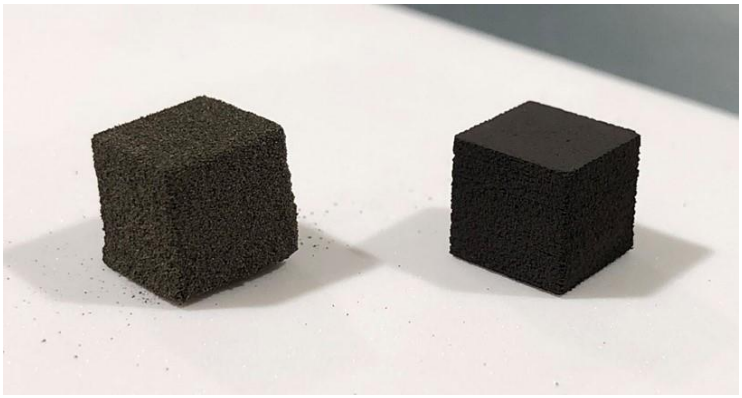

Figure 1.15 Cubes printed by ExOne X1-Lab Binder Jetting printer (8x8x8mm) Left: 100% of -106+45um Spherical Fe powder Right: 56% of -106+45um & 44% of <10um Spherical Fe powder

However, finding the optimal packing ratio by trial and error is time-consuming. A linear packing model (1.1) developed by Stovall et al. [19] can predict the final packing ratio with different powder size. It can reduce the time significantly by estimating the optimal ratio using mathematical interpretation. The model can calculate the predicted final powder packing density γ_i, with a given ratio, where the ith component in this case is the "dominant" powder ratio. For example, a mixture that contains X weight percent of powder 1 and Y weight percent of powder 2, if the weight percent of powder Y is greater than the weight percent of powder X, then i = 2, and vice versa. β_i is the relative packing density of the ith component where d_i is the average diameter of the ith component. $a_{i,j}$ and $b_{i,j}$ in Eqs. (1.2), (1.3) are the loosening and wall effect parameters respectively. y_j is the volume ratio of the jth component. Since the model does not incorporate the size distribution of each powder, the actual mixture will deviate slightly from the predicted value, and the error allowance is 10%, according to [25].

$$\gamma_i = \frac{\beta_i}{1-\sum_{j=1}^{i-1}\left[1-\beta_i+b_{i,j}\left(1-\frac{1}{\beta_i}\right)\right]y_i-\sum_{j=i+1}^{n}[1-a_{i,j}\frac{\beta_i}{\beta_j}]y_j} \tag{1.1}$$

$$a_{i,j} = \sqrt{1-\left(1-\frac{d_j}{d_i}\right)^{1.02}} \tag{1.2}$$

$$b_{i,j} = 1-\left(1-\frac{d_i}{d_j}\right)^{1.50} \tag{1.3}$$

A PYTHON code was developed to apply this equation. The equation takes the tapped density and the average powder size as input variables. A tapping device (Figure 1.16), according to the ASTM

standard [26], was made to measure the tapped density of each powder needed for the mixture. For finding the optimal packing ratio, the following process is conducted:

1. 100 grams of powder are measured on a high precision scale and put into a graduated cylinder and the volume was measured. The number is recorded as the pre-tapped density for comparison.
2. The graduated cylinder is tapped on the tapping device at 150 revolutions per minute (RPM) for at least 20 minutes to ensure the powder is tapped more than 3000 times.
3. After the tapping, the powder volume is measured again, and the tapped density data are recorded.
4. The process is repeated five times for each size powder; the data are averaged and input into the PYTHON code for calculation.
5. The predicted optimum ratio from the model is then applied on each size powder and mixed in a high-speed mixer or ball mill.
6. The mixed powder is tapped, and the packing density is then measured.
7. The actual data are then compared to the predicted data. According to Du et al. [25], the error should be in the 10% range as most of the powder on the market has a size distribution, instead of having the same diameter as the model assumes.

Figure 1.16 A custom made tapping device in accordance with the ASTM standard [26]

CHAPTER 2 NON-GRAIN ORIENTED ELECTRICAL STEEL WITH PURE ELEMENTAL POWDER APPROACH

2.1 Introduction

Electrical steel is a soft magnetic material whose main components are Iron and small amounts of Silicon ranging between 1wt.% and 6.5wt.%. According to Bozorth [27], the improvements expected by adding Silicon into mainly Iron powder includes an increase in permeability, decrease in hysteresis loss, and a reduction in eddy-current loss since the Silicon increases the electrical resistivity of Iron. The Iron-Silicon electrical steel has the following characteristics in magnetic properties: small hysteresis loop resulting in low power loss per cycle, low core loss, and high permeability. The word "soft" in the soft magnetic material means the sense of being easily magnetized and demagnetized. Usually, this kind of material has the intrinsic coercivity[3] of less than 1000 A/m. It is used for electric energy-related applications such as power generation, conversion, transfer, and condition, which are essential commodities in the modern economy [28]. In particular, there are two specified types of electric steel: grain-oriented (GO) and non-grain oriented (NGO). Grain-oriented electrical steel is processed to optimize the magnetic properties in the rolling direction. Usually, it is cold/hot rolled, which results in a specific grain orientation. They are mainly used for static applications, such as core of transformers. Figure 2.1 is the micrographic example of a cold-rolled electrical steel sheet. Non-grain oriented electrical steel does not go through a process that alters the crystal orientation, resulting in isotropic magnetic properties. An example of its micrograph is shown in Figure 2.2 It is mainly used for applications where the direction of the magnetic flux is not constant, such as making cores for motors and generators, which is more widely used in the market. Producing non-grain oriented electrical steel with the BJT process is the focus of this chapter.

[3] One of the properties of magnetic materials, often simply referred to as coercivity. It's defined as the intensity of the external magnetic field that must be applied to reduce the magnetization of the material back to zero after it has been magnetized to the saturation point.

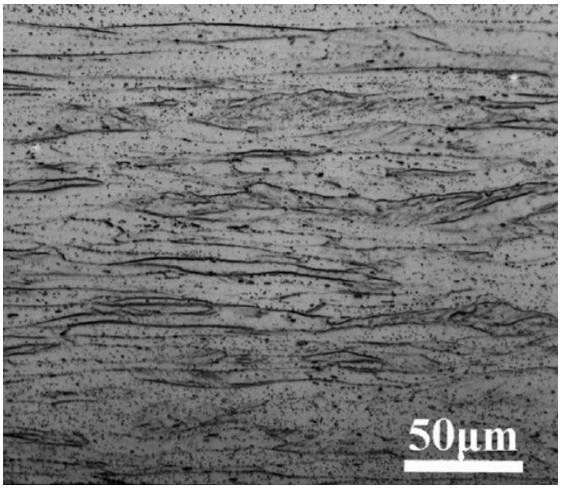

Figure 2.1 An example microstructure of an electrical steel sheet after cold rolling [29]

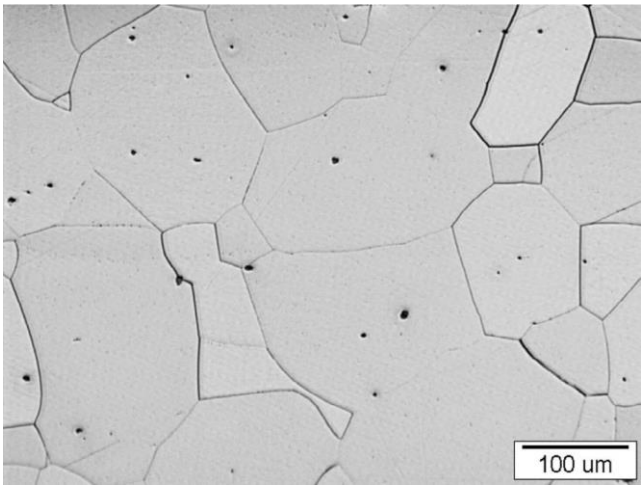

Figure 2.2 Ferrite microstructure of non-oriented, electrical steel sheet [30]

2.2 Important properties of magnetic materials

To understand the performance of electrical steel, the magnetic properties are the important factors to consider. It is necessary to introduce some basic concepts of magnetic properties. Figure 2.3 is a hysteresis loop, which shows the relationship between the applied magnetic field strength H measured in Ampere per meter (A/m) and the magnetic induction B in Tesla (T) which is also called magnetic flux density.

Permeability is usually represented by μ, which is the rate of change of the initial curve in the measure of magnetization and the applied magnetic field. The initial curve starts from the origin

and ends at the saturation point. From the hysteresis loop shown in Figure 2.3, the permeability is the initial slope of the dotted curve. The property is measured in Henries per meter (H/m). Relative permeability is an unitless property defined by the ratio of the material's permeability to the permeability of free space, μ_0, which is $4\pi\times10^{-7}$ H/m. The maximum relative permeability is the property being compared in this study.

Hysteresis loss is the energy waste by the following phenomenon. For the hysteresis loop shown in Figure 2.3, as the applied magnetizing force, H, goes to zero, the magnetic flux density of the sample, B, does not. Some additional magnetizing force in the opposite direction is needed for the magnetic induction to go to zero. The value is equal to the grey area enclosed by the hysteresis loop in Figure 2.3.

Eddy current loss is the result of Faraday's Law. When a conductive material experiences a changing magnetic field, it will circulate currents within the material's body, called eddy currents. The power loss caused by these currents is known as eddy current loss.

Anomalous loss includes any other losses besides hysteresis and eddy-current losses. This type of loss is less studied since the reason for such loss is still unknown.

Total loss is also called "Core loss," which is the sum of the three losses discussed above.

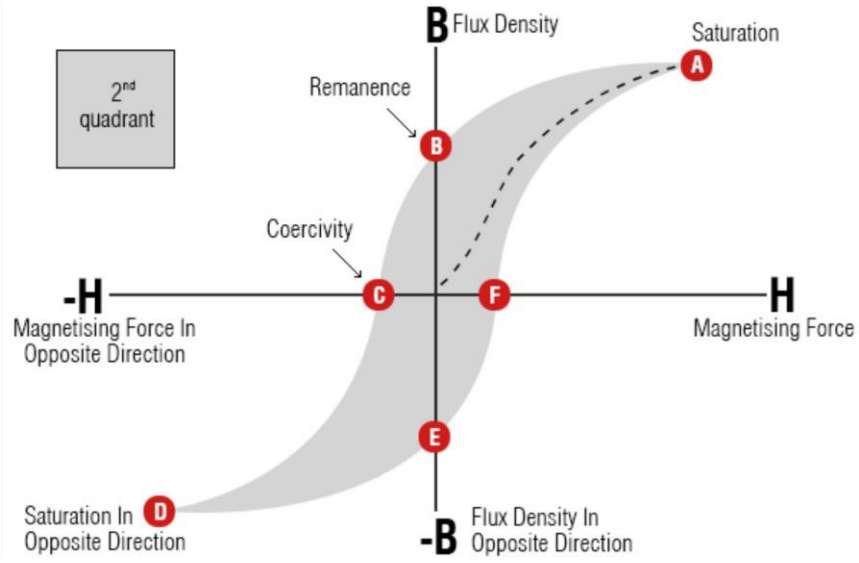

Figure 2.3 An example to illustrate a magnetic hysteresis loop [31]

2.3 State of the art

2.3.1 Commercially available electrical steels

Currently, electrical steel lamination (ESL) is the most popular method to form electrical cores. The electrical steel is rolled into sheets to 0.05~0.5 mm thickness, then cut and stacked together. They are coated with insulation adhesives between the sheets to reduce eddy current loss for specific directions. The insulation adhesives are categorized into different grades by ASTM A976 [32]. The ESL has low hysteresis loss and high relative permeability (typically greater than 4000, improved grades can have a higher maximum relative permeability). However, since the steel sheets are laminated and stacked, the joule heating created by the eddy current can only be reduced in the perpendicular of the stacked direction. Hence, the material is limited in magnetic flux in the stacked direction, and the design of electrical components using this laminated electrical steel is also limited. Another limitation is that processing electrical steel with higher Silicon content (greater than 4wt.%) is almost impossible to roll into thin sheets and cut into desired shapes due to its brittleness [33].

Another type of electrical core material is soft magnetic composites (SMCs). They are made from Iron powder particles with an electrically insulating material, which are formed by powder metallurgy. The manufacturing process allows the material to have an isotropic material property and a low eddy current loss. However, since the material is only compacted, the density and mechanical strength are extremely low, making it unfeasible for the designs to withstand significant mechanical loading. The material also has a relatively low maximum relative permeability (< 1000) [34]. The goal in producing electrical steel with BJT is to aim the mechanical and magnetic properties better than SMC and reach it close to steel lamination with the advantage of allowing a more flexible design.

2.3.2 Electrical steels by AM

Some studies have been done for processing Iron-Silicon electrical steel by additive manufacturing. Cramer et al. [1] processed $Fe_{93.5}Si_{6.5}$ with BJT and achieved 7.31 g/cc in density, 434 MPa of the ultimate tensile strength, and a maximum relative permeability of 10700. The total loss at 400Hz with 0.5T is 67.06 W/kg. The samples are sintered at 1300°C for 2 hours in a vacuum environment in the vacuum level of 10^{-5} Torr, then annealed in an H_2 environment at 800°C for 2 hours. Another

study showed that BJT processed electrical steel has a low level of magnetic anisotropy due to its isotropic densification process [35]. For other AM techniques, the SLM process is also investigated in some studies [36, 37], the results show that the magnetic property resulting from the SLM process is lower compared to commercial Iron-Silicon laminated steel. However, applying a heat treatment to SLM processed steel can significantly improve the magnetic property, The maximum relative permeability enhanced from 2000 to more than 24000 after annealing [36]. In another study, Goll et al. [38] used SLM to process $Fe_{93.3}Si_{6.7}$ and achieved the density of 7.47g/cc, the maximum permeability of 30000, and the total loss of 95.5 W/kg for 200Hz at 1.0T.

2.3.3 Elemental powder approach by BJT

The elemental powder approach in processing non-grain-oriented electrical steel uses two sizes of pure Iron powder (~99% purity) for optimal packing and pure Silicon powder (~99.99%) as an additive to adjust the Silicon content (3 wt.% ~ 5 wt.%) for liquid phase sintering. Boron was also added as a sintering additive to enhance liquid phase sintering. Because both Silicon and Boron will form eutectic compounds with Iron [39]. The analysis of variance (ANOVA) technique was used to observe the effect of three experimental factors: the sintering temperature (1200°C and 1250°C), the amount of Silicon (3 wt.% and 5 wt.%), and the amount of Boron (0 wt.% and 0.25 wt.%). Figure 2.4 and Figure 2.5 are the phase diagrams for Iron-Silicon, and Iron-Boron, respectively. It shows that the lowest eutectic temperature for Boron-Iron is 1171.4°C. The lowest eutectic temperature for Iron-Silicon is 1212°C.

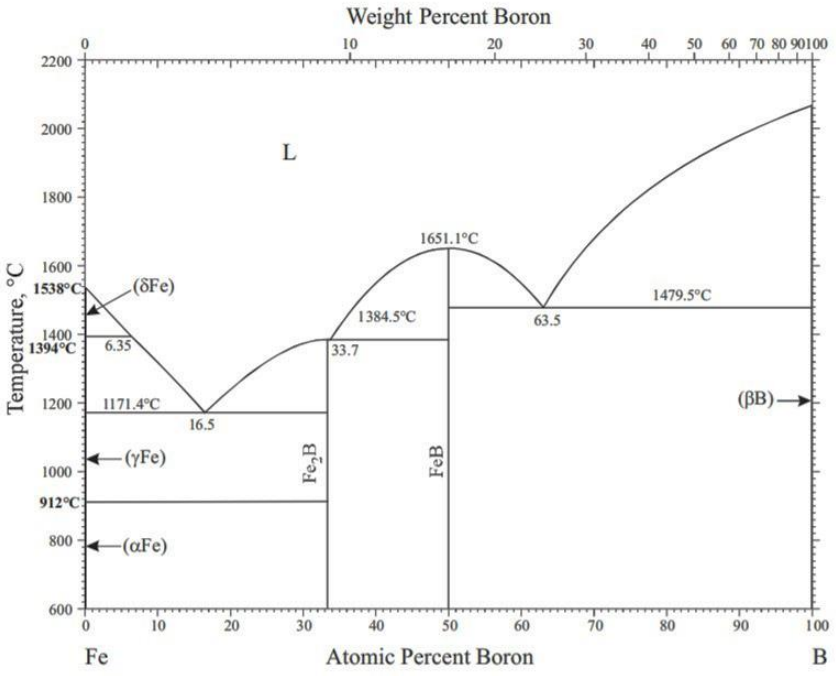

Figure 2.4 Binary phase diagram of Fe-B [39]

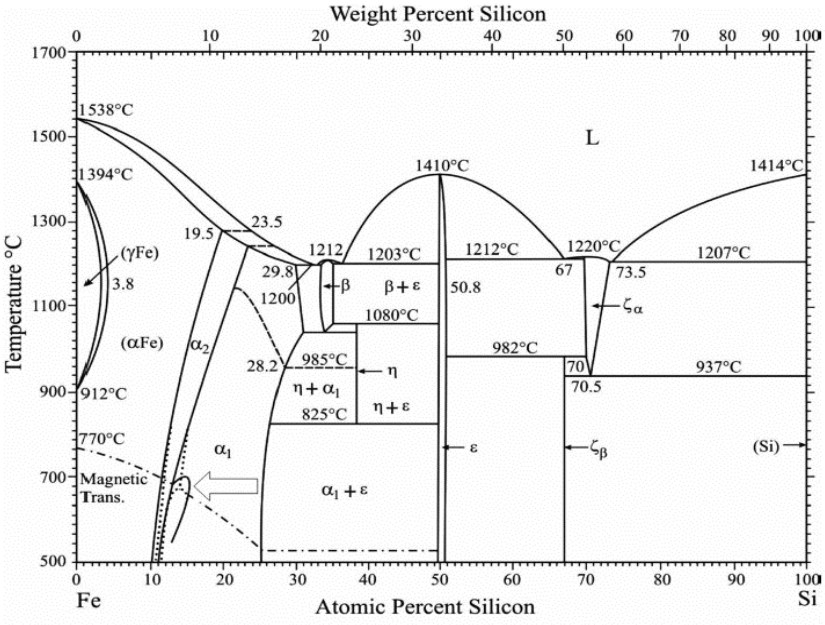

Figure 2.5 Binary phase diagram of Fe-Si [39]

2.3.4 Materials and Methods

2.3.4.1 Feed stock preparation

For this approach, the elemental powders used in this study are shown in Table 2.1. Both Iron powders were tapped, and its packing density (shown in Table 2.2) was measured and input into the linear packing model, and the graph of the model is shown in Figure 2.6. Both powders were mixed in a high-speed mixer DAC 150 from FlackTek (Landrum, SC, USA) with 1500 RPM for 100 seconds. The result (in Table 2.3) shows that the actual powder packing of the mixture is around 65.13%. Compared to the predicted packing density 66.26% from the linear packing model, the result falls inside the range of prediction (10% error allowance, according to [25]). The Iron powder is then mixed with the Silicon and Boron powder in a desired ratio.

Table 2.1 Powder used in this chapter of study

Element	Average powder size	Claimed purity	Company
Fe	90 µm	~99%	American Elements (CA, USA)
Fe	10 µm	≥99.9%	Sigma Aldrich (MO, USA)
Si	1 µm	99.99%	US Research Nanomaterials (TX, USA)
B	1 µm	≥95%	Sigma Aldrich (MO, USA)

Table 2.2 Measured tapped density of the metal powders

Element	Powder size	Average tapped density (g/cc)	Relative Density to 7.874 g/cc
Fe	90 µm	3.5684	45.32%
Fe	10 µm	4.1426	52.61%

Table 2.3 Result comparison between the linear packing model & the actual mixture: Elemental powder

Fe Mixture	-106+45 µm (wt.%)	<10 µm (wt.%)	Relative packing
Packing model	55.5	44.5	66.26%
Actual Mixture	56	44	65.13%

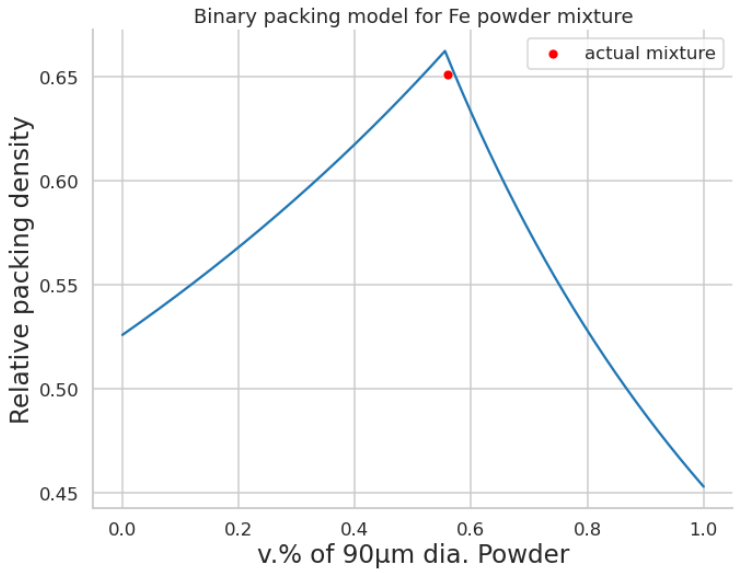

Figure 2.6 Powder packing density with different v.% of 90 μm powder, the red dot indicates the value of the actual powder mixture

2.3.4.2 Sample preparation

A BJT printer X1-Lab from ExOne (North Huntington, PA, USA) was used to print the rings to measure magnetic properties and the cubes for cross-sectional analysis. The detailed printing process is described in chapter 1.3.1. The printing parameter for the samples is set to the feed powder ratio of 2.3:1 and the layer thickness of 150 μm. The saturation rate is 70%, assuming 60% of powder packing density. Furthermore, the initial rolling speed is set to be 0.3 millimeters per second. After printing, the green parts were placed in an air furnace at 195°C for 2 hours for curing. Then the samples were sintered in a carbon lined resistance furnace (Material research furnaces MRF T-16X26-G-G-3000-VM-G, Allenstown, NH) shown in Figure 1.10. The furnace chamber is vacuumed and purged by Argon three times to reduce oxygen content. Then the chamber was filled to 906 Torr with Argon and increased to the respective sintering temperature with the ramp rate of 5°C/min. After dwelling for 6 hours, each sample was cooled at approximately 15°C/min. In total, a set of eight samples was made. The details of each sample are shown in Table 2.4, and the pictures of the printed and sintered samples are shown in Figure 2.7. After sintering, the density of each sample is measured by the Archimedes method. The ring samples are prepared for magnetic characterization. The cube samples are sectioned, mounted, and polished for cross-sectional analysis. The detailed results are presented in the following sections.

Table 2.4 The processing variables of each set of samples

Sample Number	Silicon content (wt.%)	Boron addition (wt.%)	Sintering Temperature (°C)
1	3	0.00	1200
2	3	0.25	1200
3	5	0.00	1200
4	5	0.25	1200
5	3	0.00	1250
6	3	0.25	1250
7	5	0.00	1250
8	5	0.25	1250

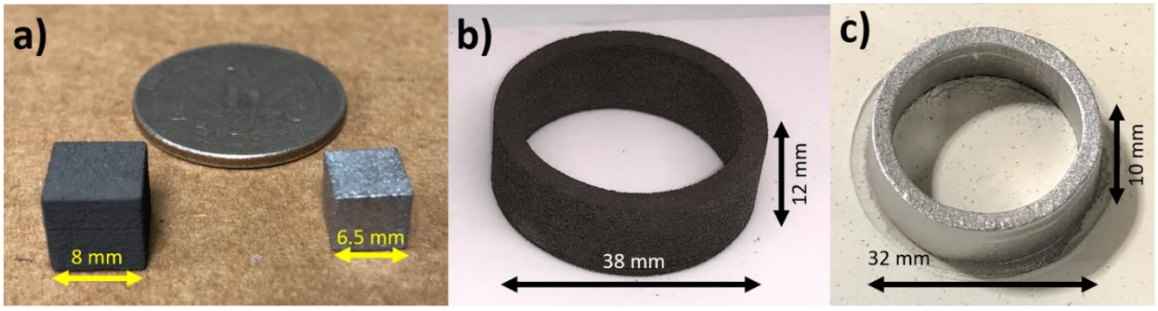

Figure 2.7 a) printed cube (left) vs a sintered cube (right) b) As printed ring sample c) Sintered ring sample

2.3.4.3 Magnetic Characterization

Both direct current (DC) and alternating current (AC) magnetic characterization techniques were used to measure the magnetic performance of the prepared samples. The experimental setup consists of a ring core test based on two standards: ASTM A773 “Standard Test Method for Direct Current Magnetic Properties of Low Coercivity Magnetic Materials Using Hysteresigraphs” [40] and ASTM A927 “Standard Test Method for Alternating-Current Magnetic Properties of Toroidal Core Specimens Using the Voltmeter-Ammeter-Wattmeter Method” [41] for DC and AC measurements. The equipment used is a commercially available soft magnetic tester (Magnetic

Instrumentation Model SMT-700) whose schematic is shown in Figure 2.8. For each ring sample, the primary windings include 100 turns, and the secondary windings include 75 turns. A current shunt was used to measure the excitation current amplitude in the primary windings and calculate the sample's magnetic field strength H.

For the DC characterization the quasi-static sinusoidal excitation at 1 Hz was used for the primary windings. The extracted magnetic properties for the DC characterization include the maximum relative permeability, $\mu_{r,max}$; the intrinsic coercivity, H_c; the hysteresis loss with the magnetic induction of 1.5T.

For the AC characterization, the specific loss density of each sample was extracted at excitation frequencies at 400 Hz with the induction of 0.5T. Closed-loop control ensured that for each frequency the secondary induced voltage remained sinusoidal, having a form factor within the range of 1.11 ± 1%. The form factor was defined as the ratio between the average rectified value (the average of its absolute value) of the secondary voltage and the root-mean square of the secondary voltage [41].

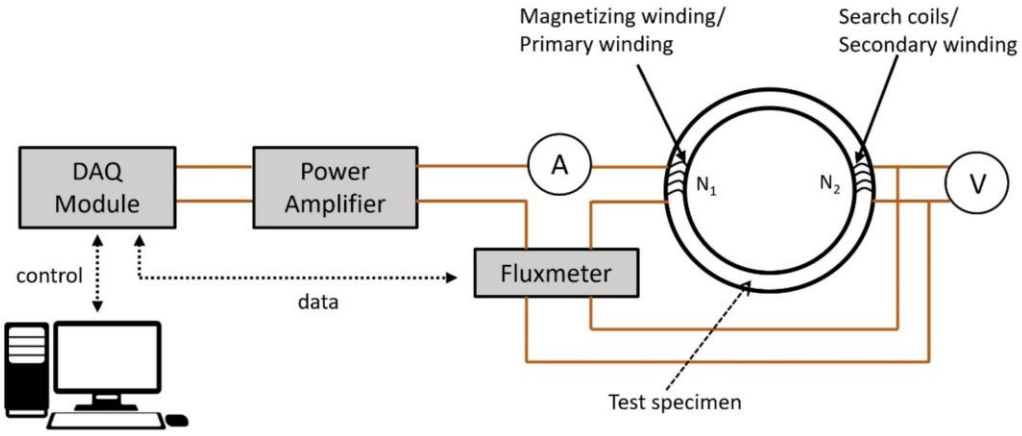

Figure 2.8 A schematic of the DC/AC magnetic characterization for the ring core [42]

2.3.4.4 Metallography

All sintered samples were cut, mounted, and metallographically prepared for microstructural evaluation. Samples were mechanically polished using a series of 400, 600, 800, and 1200 US grit size (equivalent to FEPA 800, 1200, 2400, and 4000 grit, respectively) SiC abrasive papers followed by diamond polishing with polycrystalline diamond paste with a series of particle sizes

of 6, 3, 1, and ¼ μm with isopropyl alcohol as the lubricant. The final polishing was performed using colloidal silica solution (0.025 μm crystallite size 50% diluted with IPA).

2.3.4.5 Sample characterization

Optical microscopy (OM) and scanning electron microscopy (SEM) are used to characterize the microstructures. A Nikon Eclipse MA200 optical microscope was used to take images for calculating the average grain size using the line intercept method as per ASTM-E11213 [43]. Backscattered electron (BSE) images were acquired by Tescan Mira3 FEGSEM for micrograph comparison. The typical SEM imaging conditions included a 20 keV beam voltage, a 17-mm working distance, and a 20nm spot size. Energy dispersive spectroscopy (EDS) analysis was performed to investigate the composition of the phases inside the SEM using an acceleration voltage of 20 kV at a working distance of 12 mm. A Clark CM-800 AT hardness machine was used to determine Vickers microhardness values on various locations of the samples with a load of 0.2 kilogram-force and a dwell time of 15s. The densities of the samples were measured by Archimedes' principle in 99.5% isopropyl alcohol.

2.3.4.6 Analysis of variance (ANOVA)

Analysis of variance (ANOVA) was used to efficiently investigate the effects of processing variables for the material. It is a statistical tool to analyze the difference among means. It is used to interpret the collected magnetic and microstructural characteristics. Since the 50°C temperature range is narrow, for each output response, the temperature factor was tested as a one-way ANOVA first to determine if it has a significant impact (Table 2.5). If temperature does have a significant impact, the 8 sets of samples can be treated as a 3-factor (Silicon content, Boron content, and sintering temperature), 2-level design of experiment (DOE) with one replicate. If the temperature does not have a significant impact on the response, the 8 sets of samples can be interpreted as a 2-factor (Silicon content, Boron content), 2-level DOE with two replicates. By using the equations in Table 2.6 to analyze the variance of the two-factor factorial design with two replicates, The F value, F_0, can be calculated, and the P value can be found with the F distribution table. The significance level 0.05 was used for testing the hypothesis shown in equation (2.1). The first hypothesis is the null hypothesis (H_0), meaning that all the responses are equal. There is no significant difference between the results; the tested factor does not have a significant impact on

the response. The alternative hypothesis, H_a, means that at least one response is not equal to the others, stating that the tested factor has a significant impact on the response. If the P value is smaller than the significance value 0.05, the null hypothesis is rejected, the alternative hypothesis is accepted, meaning that the factor has a significant impact on the response. If the P value is larger than the significance value 0.05, the null hypothesis is accepted, meaning that the factor has an insignificant impact on the response.

Table 2.5 ANOVA table for on the selected measured output. The variation in temperature is the input factor

Source	Degrees of freedom	Sum of squares	Mean squares	F_0
Temperature	$k-1$	$SS_{Temperature}$	$MS_{Temperature}$	$F_0 = \frac{MS_{Temperature}}{MS_E}$
Error	$n-k$	SS_E	MS_E	
Total	$n-1$	SS_T		

Table 2.6 Two-factor ANOVA table on the selected measured output. The variation in Silicon and Boron are the two input factors

Source	Degrees of freedom	Sum of squares	Mean square	F_0
Si	$a-1$	SS_{Si}	MS_{Si}	$F_0 = \frac{SS_{\mathrm{Si}}}{MS_{\mathrm{B}}}$
B	$b-1$	SS_{B}	MS_{B}	$F_0 = \frac{SS_{\mathrm{B}}}{MS_E}$
Interaction	$(a-1)(b-1)$	$SS_{\mathrm{Si{\cdot}B}}$	$MS_{\mathrm{Si{\cdot}B}}$	$F_0 = \frac{SS_{\mathrm{Si{\cdot}B}}}{MS_E}$
Error	$ab(n-1)$	SS_E	MS_E	
Total	$abn-1$	SS_T		

Table 2.7 The description of a two-factor factorial design with two replicates

Silicon Content	Boron content	Measured output	
3.00%	0.00%	$y1,1,1$	$y1,1,2$
3.00%	0.25%	$y1,2,1$	$y1,2,2$
5.00%	0.00%	$y2,1,1$	$y2,1,2$
5.00%	0.25%	$y2,2,1$	$y2,2,2$

$$\begin{cases} H_0 : \mu_1 = \cdots = \mu_k \\ H_a : \exists\, i,j : \mu_i \neq \mu_j \end{cases} \tag{2.1}$$

2.3.5 Results

The ANOVA results in Table 2.8a show that the P-value is 0.428. Since the α value was set to be 0.05, it makes the null hypothesis accepted, which means that 50°C temperature difference does not have a significant impact on these samples. Hence, the DOE became a 2^2-factorial design with two replicates. Table 2.8b shows that none of the P-values for Boron, Silicon, and the interaction between them is smaller than the significant level of 0.05, meaning that all three input factors have an insignificant impact on density.

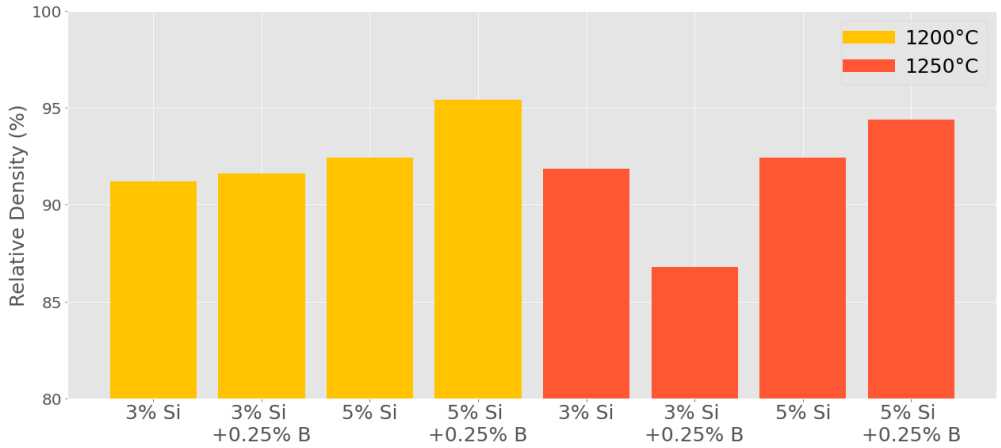

Figure 2.9 Density comparison between elemental powder mixture (The higher, the better.)

Table 2.8 ANOVA for the impact on density

(a) Impact from temperature

Analysis of Variance

Source	DF	Adj SS	Adj MS	F-Value	P-Value
Temp	1	3.380	3.380	0.48	0.514
Error	6	42.228	7.038		
Total	7	45.608			

(b) Impact from Boron & Silicon

Analysis of Variance

Source	DF	Adj SS	Adj MS	F-Value	P-Value
Boron	1	0.0128	0.0128	0.00	0.952
Silicon	1	21.6482	21.6482	7.05	0.057
Boron*Silicon	1	11.6645	11.6645	3.80	0.123
Error	4	12.2825	3.0706		
Total	7	45.6080			

The results shown in Table 2.9a again indicate that the sintering temperature does not have a significant impact on the maximum relative permeability. Table 2.9b shows that Boron has a P-value of 0.024, Silicon has a P-value of 0.042, and the interaction between them has a P-value of 0.027. This means all three of them significantly impact maximum relative permeability. The interaction plot of Figure 2.11 indicates that additional Boron has a negative impact with 3 wt.% of Silicon. Figure 2.10 shows that both samples with 3wt.% of Silicon with 0.25wt.% of Boron have low values in maximum relative permeability with the sintering temperatures of 1200°C and 1250°C.

Table 2.10a again shows that the sintering temperature does not have a significant impact on hysteresis loss. The repeating results on temperature do not impact on any properties, indicating that the 50°C temperature range is too narrow for this DOE to see the effect of the sintering temperature. Boron and Silicon contents have a significant impact on hysteresis loss at 1.5T. However, the interaction between Silicon and Boron does not. The interaction plot Figure 2.13 indicates that both Boron and Silicon reduce the hysteresis loss.

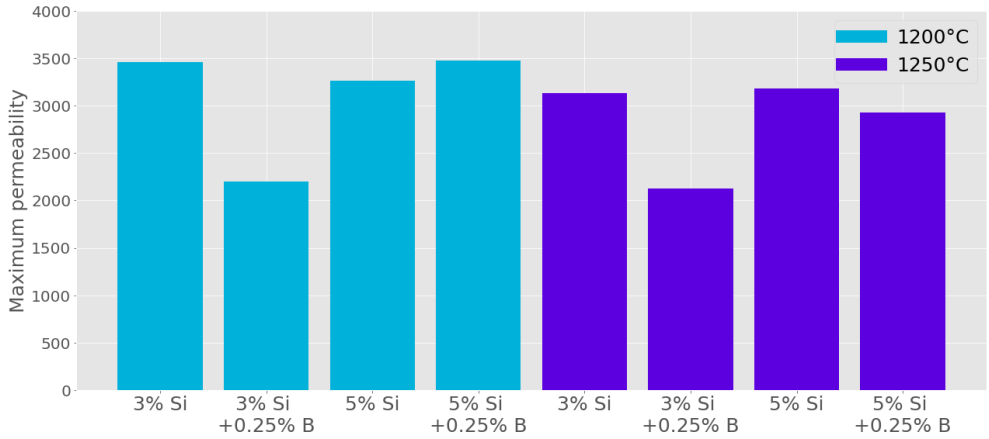

Figure 2.10 Maximum relative permeability comparison between elemental powder mixture (The higher, the better.)

Table 2.9 ANOVA for the impact on maximum relative permeability

(a) Impact from temperature

Analysis of Variance

Source	DF	Adj SS	Adj MS	F-Value	P-Value
Temp	1	133903	133903	0.44	0.532
Error	6	1827030	304505		
Total	7	1960933			

(b) Impact from Boron & Silicon

Analysis of Variance

Source	DF	Adj SS	Adj MS	F-Value	P-Value
Boron	1	668746	668746	12.62	0.024
Silicon	1	460320	460320	8.69	0.042
Boron*Silicon	1	619941	619941	11.70	0.027
Error	4	211926	52981		
Total	7	1960933			

The total loss presented on Table 2.11b shows that only Silicon impacts the total loss at 0.5T for 400Hz. The effect of Boron and the interaction between Boron and Silicon have no impact. The interaction plot presented in Figure 2.15 shows that Silicon reduces the total loss. Boron itself has a significant impact on grain size as shown in Table 2.12b. Silicon and the interaction between Boron and Silicon does not have a significant impact on the grain size. The interaction plot Figure 2.17 shows that Boron increases the grain size significantly. Furthermore, for hardness, only the interaction between Boron and Silicon is insignificant (Table 2.13b). Both elements increase the hardness according to the result plot Figure 2.18 and the interaction plot Figure 2.19.

Figure 2.20 shows that for the samples sintered at 1200°C, both amounts of Silicon, not only the smaller pores within the grains are reduced but also the grain size is significantly increased with Boron addition. It indicates that 0.25 wt.% of Boron is more efficient for liquid phase sintering.

However, the large pores in $Fe_{97}Si_3$ are more apparent than in other combinations. The reduction in maximum relative permeability could be the outcome of this microstructure. Similar conclusions can be drawn from the set of samples sintered at 1250°C in Figure 2.21.

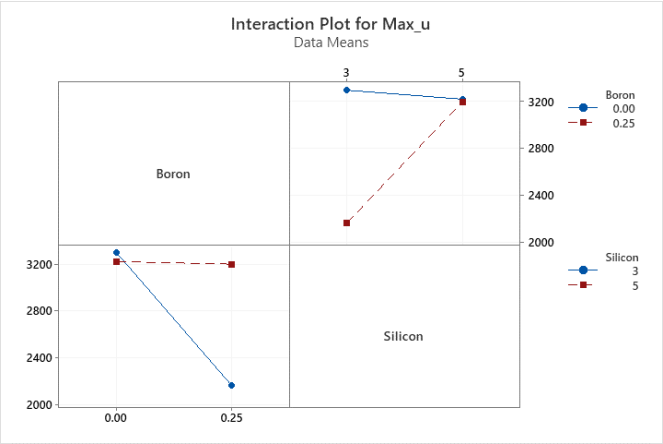

Figure 2.11 Interaction plot of Silicon and Boron for maximum permeability (data means)

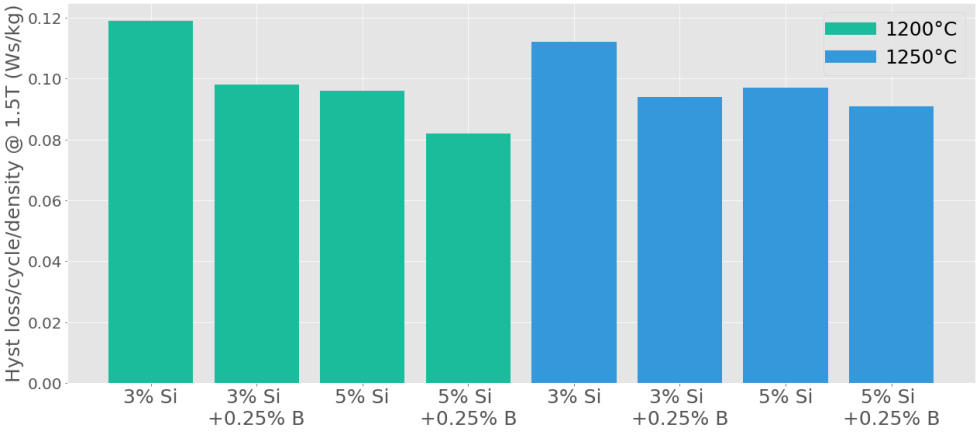

Figure 2.12 Hysteresis loss comparison between elemental powder mixture at 1.0T (The lower, the better.)

Table 2.10 ANOVA for the impact on hysteresis loss at 1.5T

(a) Impact from temperature

Analysis of Variance

Source	DF	Adj SS	Adj MS	F-Value	P-Value
Temp	1	0.000003	0.000003	0.02	0.890
Error	6	0.000897	0.000149		
Total	7	0.000900			

(b) Impact from Boron & Silicon

Analysis of Variance

Source	DF	Adj SS	Adj MS	F-Value	P-Value
Boron	1	0.000351	0.000351	9.65	0.036
Silicon	1	0.000325	0.000325	8.94	0.040
Boron*Silicon	1	0.000078	0.000078	2.15	0.217
Error	4	0.000146	0.000036		
Total	7	0.000900			

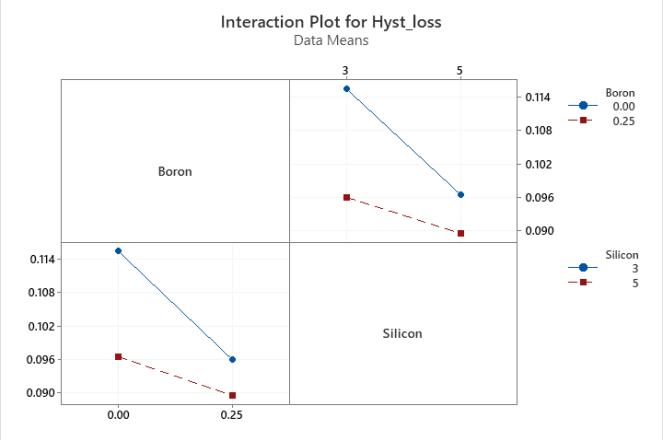

Figure 2.13 Interaction plot of Silicon and Boron for hysteresis loss at 1.0T (data means)

2.3.6 Discussion

ANOVA shows that the sintering temperature range between 1200°C and 1250 °C does not show the impacts on the measured properties. A wider range is needed to see the effect of the sintering temperature. For 3wt.% of Silicon, the additional Boron reduces maximum permeability. The micrograph of Figure 2.20 indicates that the pores in $Fe_{97}Si_3$ with 0.25 wt.% of Boron is larger compared to other combinations, which indicates that 3 wt.% of Silicon with 0.25 wt.% of Boron has the negative impact on density. For both temperatures, $Fe_{97}Si_3$ with 0.25 wt.% of Boron performs poorly in maximum permeability. The same combination has the highest total loss at 0.5T for 400 indicating that this combination either has reached a critical point for eutectic formation or interacting phase change between Silicon and Boron. Further investigation is needed to identify the interacting phases in future study. Boron increases the grain size significantly, showing that the Boron additive is efficient for forming liquid phase [44], closing the smaller pores within the grain,

and benefits the material by reducing the hysteresis loss. Hardness is increased with the increase in Silicon and Boron contents. However, since AM process electrical steels do not require rolling and punching, it is not an issue in manufacturing. $Fe_{95}Si_5$ with 0.25 wt.% Boron performed the best among all combinations. By comparing with SMC in Figure 2.22, the BJT processed electrical steel has a significantly lower hysteresis loss than SMC. The core loss of the BJT processed electrical steel is low but less significant due to the nature of how SMC is made, the insulating binder between powders reduced eddy current generation.

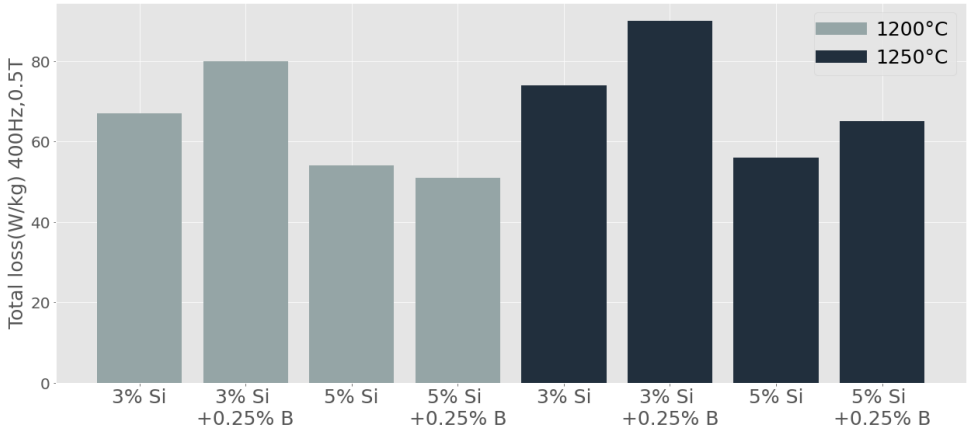

Figure 2.14 Total loss at 400Hz, 0.5T comparison between elemental powder mixture at 1.0T (The lower, the better.)

Table 2.11 ANOVA for the impact on Total loss at 400Hz, 0.5T

(a) Impact from temperature

Analysis of Variance

Source	DF	Adj SS	Adj MS	F-Value	P-Value
Temp	1	136.1	136.1	0.70	0.434
Error	6	1160.8	193.5		
Total	7	1296.9			

(b) Impact from Boron & Silicon

Analysis of Variance

Source	DF	Adj SS	Adj MS	F-Value	P-Value
Boron	1	153.13	153.13	3.51	0.134
Silicon	1	903.12	903.12	20.70	0.010
Boron*Silicon	1	66.13	66.13	1.52	0.286
Error	4	174.50	43.62		
Total	7	1296.88			

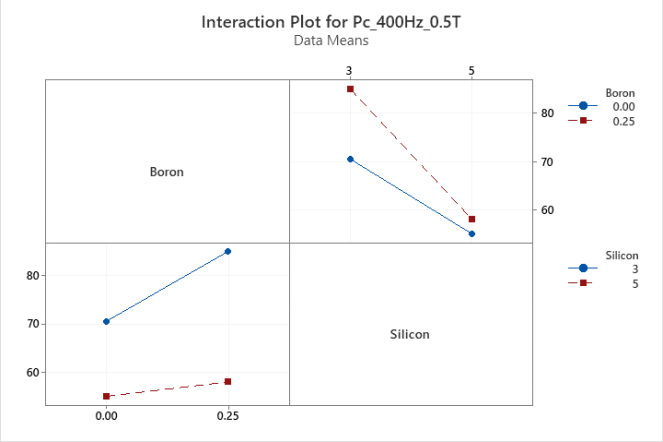

Figure 2.15 Interaction plot of Silicon and Boron for Total loss at 400Hz, 0.5T (data means)

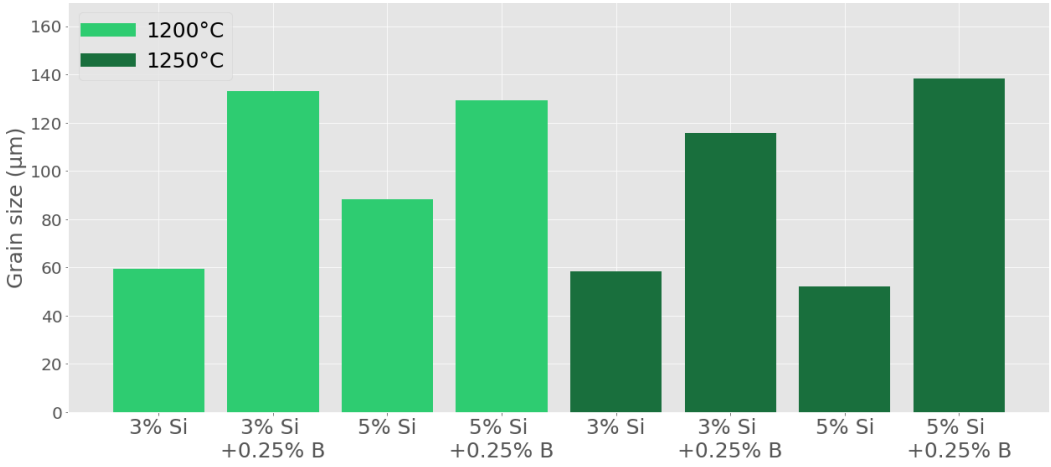

Figure 2.16 Grain size comparison between elemental powder mixture

Table 2.12 ANOVA for the impact on grain size

(a) Impact from temperature

Analysis of Variance

Source	DF	Adj SS	Adj MS	F-Value	P-Value
Temp	1	257.1	257.1	0.17	0.695
Error	6	9131.2	1521.9		
Total	7	9388.3			

(b) Impact from Boron & Silicon

Analysis of Variance

Source	DF	Adj SS	Adj MS	F-Value	P-Value
Boron	1	8326.65	8326.65	39.46	0.003
Silicon	1	215.99	215.99	1.02	0.369
Boron*Silicon	1	1.66	1.66	0.01	0.934
Error	4	843.96	210.99		
Total	7	9388.27			

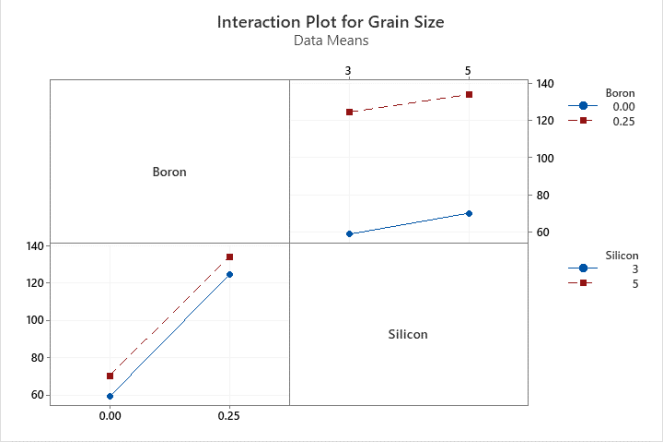

Figure 2.17 Interaction plot of Silicon and Boron for grain size (data means)

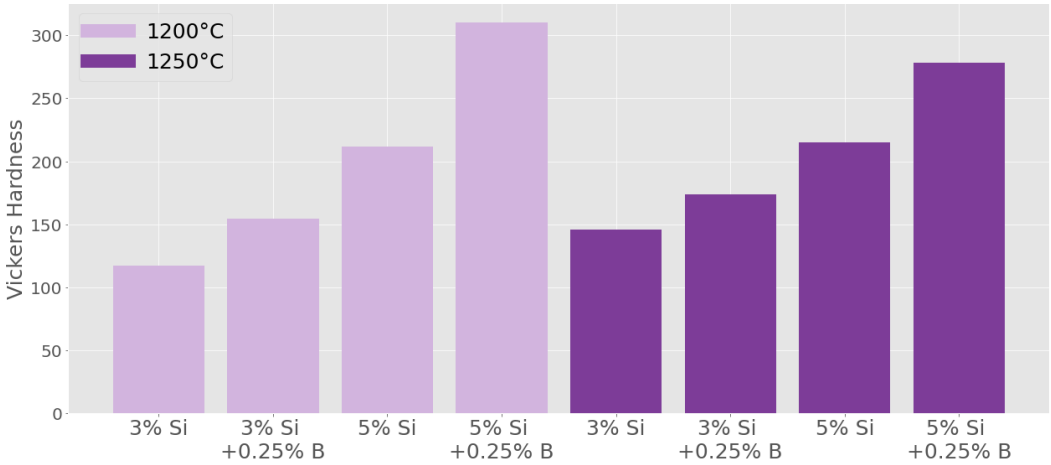

Figure 2.18 Vickers hardness comparison between elemental powder mixture

Table 2.13 ANOVA for the impact on hardness

(a) Impact from temperature

Analysis of Variance

Source	DF	Adj SS	Adj MS	F-Value	P-Value
Temp	1	46.6	46.61	0.01	0.928
Error	6	31106.1	5184.35		
Total	7	31152.7			

(b) Impact from Boron & Silicon

Analysis of Variance

Source	DF	Adj SS	Adj MS	F-Value	P-Value
Boron	1	6444	6444.0	23.23	0.009
Silicon	1	22441	22441.3	80.91	0.001
Boron*Silicon	1	1158	1158.0	4.18	0.111
Error	4	1109	277.4		
Total	7	31153			

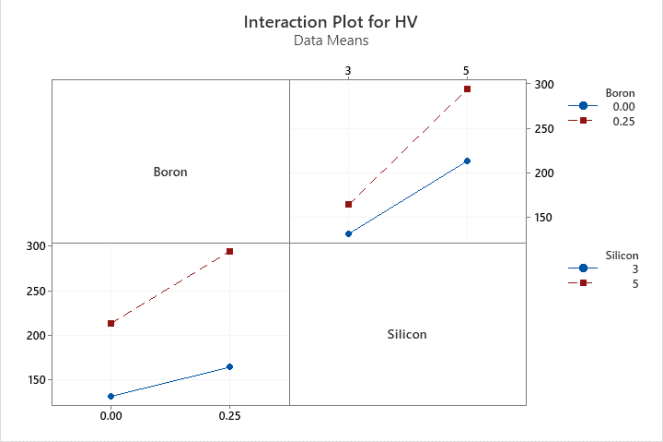

Figure 2.19 Interaction plot of Silicon and Boron for hardness (data means)

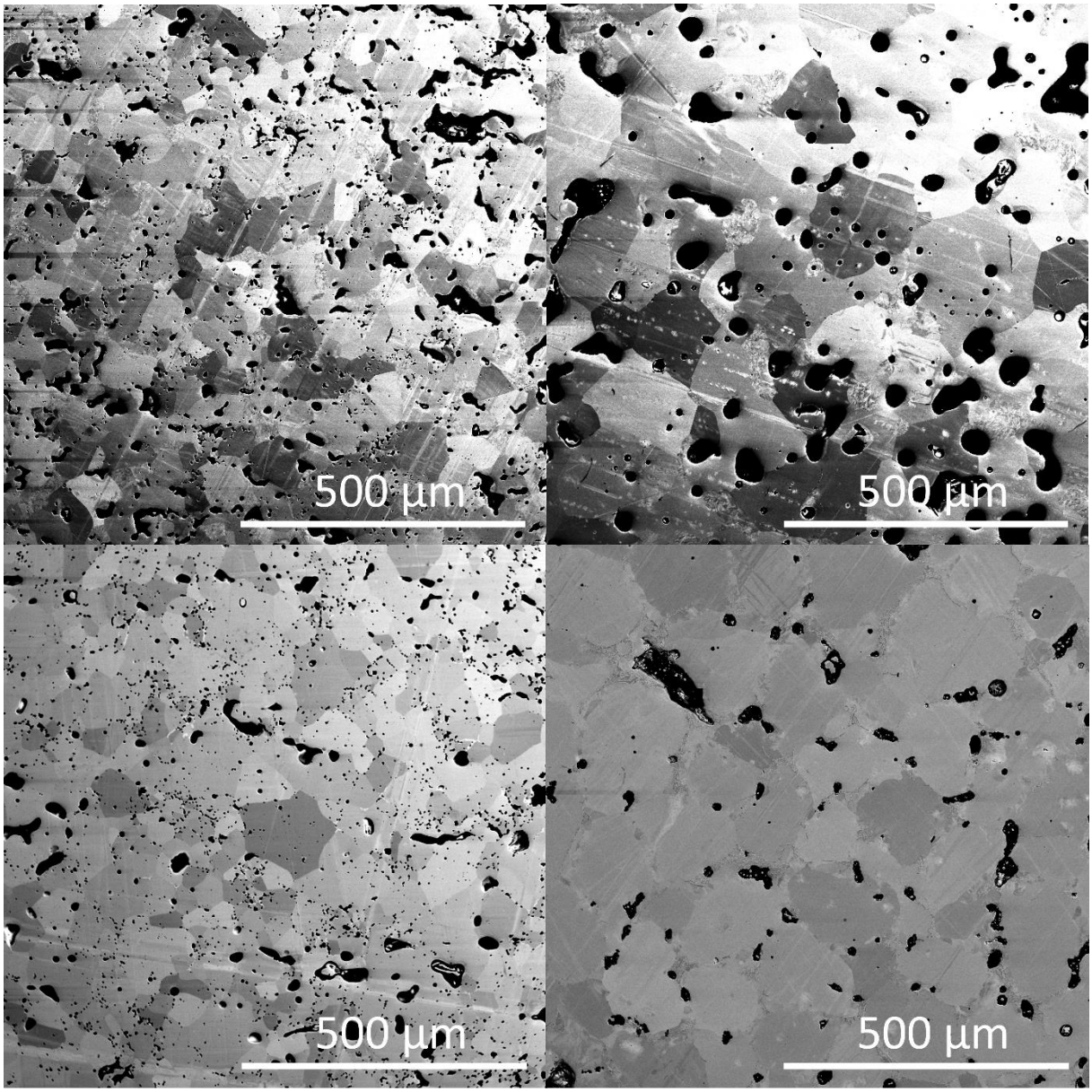

Figure 2.20 Backscatter electron image for samples sintered at 1200°C, Argon environment
top left: $Fe_{97}Si_3$, top right: $Fe_{97}Si_3$ + 0.25 wt.% Boron
bottom left: $Fe_{95}Si_5$, bottom right: $Fe_{95}Si_5$ + 0.25 wt.% Boron

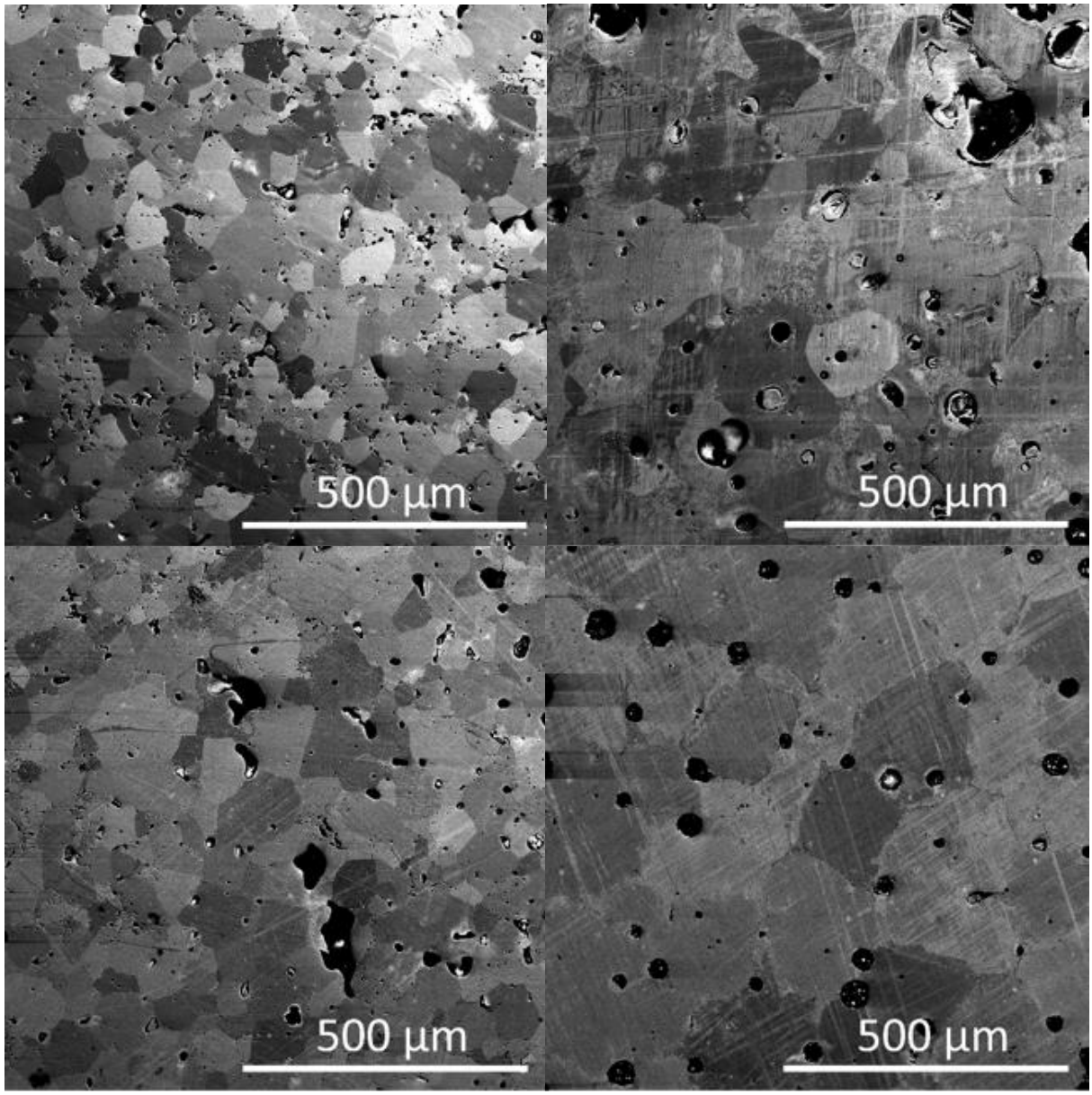

Figure 2.21 Backscatter electron image for samples sintered at 1250°C, Argon environment
top left: $Fe_{97}Si_3$, top right: $Fe_{97}Si_3$ + 0.25 wt.% Boron
bottom left: $Fe_{95}Si_5$, bottom right: $Fe_{95}Si_5$ + 0.25 wt.% Boron

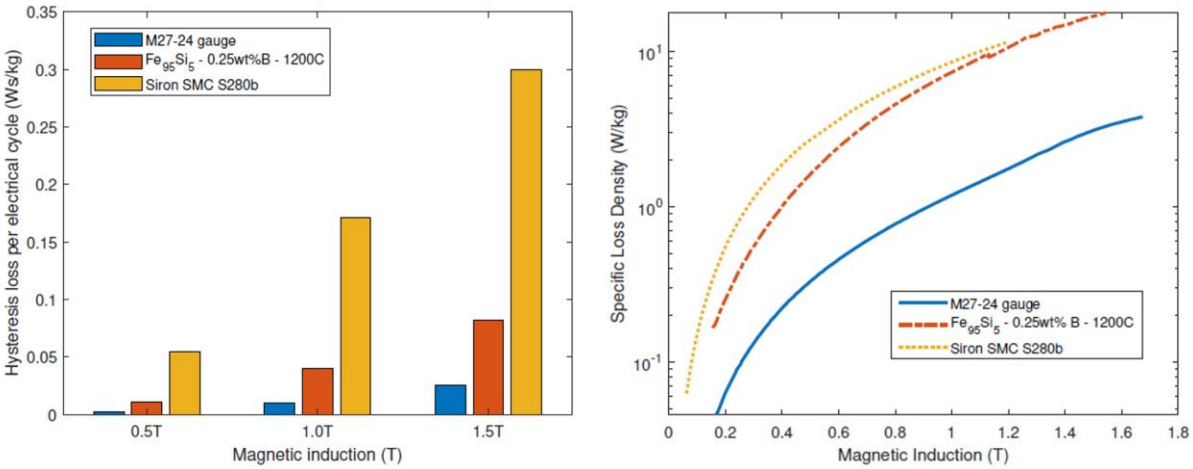

Figure 2.22 Hysteresis loss and specific loss density comparison between M27-24 gauge, $Fe_{95}Si_5$ + 0.25 wt.% B 1200C & Siron SMC S280 [45]

CHAPTER 3 NON-GRAIN ORIENTED ELECTRICAL STEEL WITH ALLOYED POWDER APPROACH

3.1 Introduction

The previous chapter shows that Boron is an effective sintering additive in forming the liquid phase. But for the sample with 3 wt.% Silicon content, additional 0.25 wt.% Boron additive has a negative effect on density and magnetic properties. The ANOVA for maximum permeability shows that using Silicon and Boron together as additives during sintering adversely impacted the magnetic performance. In this chapter, only Boron was used as a sintering additive. Instead, a pre-alloyed powder of $Fe_{92}Si_8$ was used with the pure Iron powders to re-adjust the Silicon content to around 5 wt.%. The average size of the pure Iron powder is smaller to improve the packing after printing according to the linear packing model. The results of this alloy powder approach were compared with the results from the elemental powder approach. Moreover, a wider temperature range was used in this chapter further to identify the effect of sintering temperature.

3.2 Experiment setup

3.2.1 Materials

Three powders in total were used to fabricate the samples. The material and powder sizes are presented in Table 3.1. The smaller Iron powder fills the interstitial space to improve the packing ratio, leading to the final part with a higher density than single-sized powder. The mixing ratio of the powder is found by using the linear packing model from the study by Stovall et al. [19]. Boron as a sintering additive was used to achieve liquid phase sintering. Different amounts of Boron were added to determine the improvement on density and magnetic properties.

Table 3.1 List of powder and sintering additive materials

Powder	Average Particle Size (μm)	Company
$Fe_{92}Si_8$	30	Carpenter Additive (Widnes, UK)
Fe	10	Sigma Aldrich (St. Louis, MO)
B	1	Sigma Aldrich (St. Louis, MO)

3.2.2 Powder stock preparation

By using a customized setup introduced in chapter 1.5.2, the tapped packing density of the powders was measured. The measured values were then inputted into the linear packing model to determine the optimal mixing ratio. The powders were weighed by a high-precision lab scale Adventurer™ from OHAUS corp. (Parsippany, NJ), then mixed using a high-speed mixer DAC150, manufactured by FlackTek, Inc. (Landrum, SC) at 1500 RPM for 100 seconds. The mixtures' tapped density was then measured with the tapping setup and compared with the analytical result. Once the results were confirmed to improve the powder packing, the ratio is used for the powder stock. 67 wt.% of Iron-Silicon powder, 33 wt.% of pure Iron powder, and a set amount of Boron powder were mixed. The starting powder is prepared prior to printing.

3.2.3 Part printing & sintering

A BJT printer from X1-Lab (ExOne, Huntington, PA) was used to print cube and ring samples for subsequent measurements and analysis. The detailed printing process is described in Chapter 1, Section 1.3.1. The layer thickness was set to 100 μm, and the initial spreading speed of the powder was 0.3mm/s. The powder feed ratio was set to 2.1:1. A ring with a 38 mm outer diameter, 30 mm inner diameter and 4 mm height was printed for magnetic characterization (Figure 3.1). 8 mm x 8 mm x 8 mm cubes were also printed for cross-sectional analysis and a 60 mm x 40 mm x 30 mm block was printed for tensile testing. The printed part (or green part) is then cured in an air furnace at 195 °C for two hours to cure the binder phase fully. A fully cured sample improves the printed part's structural integrity, preventing any damage while handling the samples. After curing the binder phase, the samples were placed in an environment-controlled resistance furnace (Materials Research Furnaces, Model G-3000, Allenstown, NH, USA). The chamber is vacuumed and purged with Argon three times to ensure low oxygen content. After being filled with ultra-high purity Argon (99.999%) to 906 Torrs, the chamber is heated to a set temperature at a 5°C per minute ramp rate and held at that temperature for six hours. After that, the printed parts are furnace cooled to room temperature.

Figure 3.1 Photo of an as printed ring(left), and a sintered ring(right)

3.2.4 Sample characterization

The magnetic characterization for the ring samples is the same as described in Chapter 2, Section 2.3.4.3. The density of each sample was measured with Archimedes' principle by using ~99.5% isopropyl alcohol. A Tescan Mira3 field emission gun SEM was used for back scattered electron imaging at 20 kV and with the working distance around 15 mm. Energy dispersive X-ray (EDX) analysis was done by JEOL 6610 electron microscope with 20 kV for elemental analysis.

3.2.5 Metallography

The cube samples were sectioned by cutting with the diamond saw at low speed and mounted in glass filled epoxy with 4200 psi at 180°C for 2 minutes. Then mechanically polished using a set of 400, 600, 800, and 1200 US grit size (equivalent to FEPA 800, 1200, 2400, and 4000 grit respectively) SiC abrasive papers followed by alumina suspension with the particle size 1μm and 0.3μm. Then, the final polishing was performed using colloidal silica solution (0.06 μm crystallite size and 50% diluted with ethanol).

3.2.6 Tensile testing

Due to the limited printed bed size, a 60 mm x 40 mm x 30 mm block was sintered then sectioned by wire EDM into small tensile samples shown in Figure 3.2, the cross-section measurement was done by a caliper and the test samples was pulled by Criterion Model 43 manufactured by MTS (Eden Prairie, MN) with a 0.25 mm/min displacement rate according to ASTM standards [46]. Only the ultimate tensile strength was recorded since the samples were too small for testing the yield strength. Four samples in total were tested, whose ultimate tensile strengths were to be averaged.

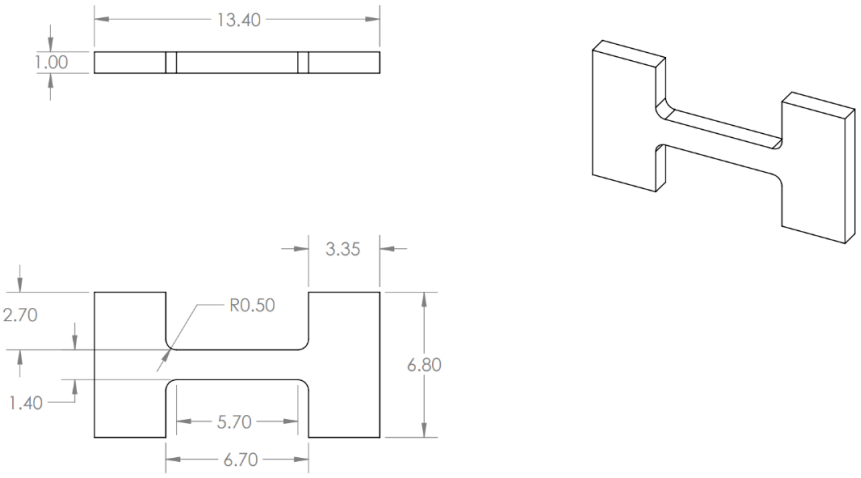

Figure 3.2 Dimensions for the mini tensile bar (in mm)

3.3 Results

The tapped density of each size powder is shown in Table 3.2. The output curve from the linear packing model is shown in Figure 3.4. The tapped density of the actual mixture is shown in Table 3.3 — the pre-alloyed powder has a relative packing density of 59.88% and the smaller Iron powder has a tapped density of 52.61%. The tapped density and the average powder size were input into the linear packing model; the results show the optimal mixing ratio is 67.28 wt.% of the alloyed powder and 32.72 wt.% of the smaller pure Iron powder. The predicted packing ratio of the mixture by the linear packing model is 67.00%, and the actual packing density after being tapped is measured at 61.97%, which falls within the error range of the linear packing model. The backscatter electron image (Figure 3.3) shows that introducing a smaller Iron particle can reduce porosity even at a lower sintering temperature as the linear packing model predicted.

Table 3.2 Measured tapped density for each powder size

Composition	Average powder size (μm)	Tapped density (g/cc)	Relative Density
Fe	10	4.1426	52.61%[4]
$Fe_{92}Si_8$	30	4.4494	59.88%[5]

[4] Density for pure iron, 7.874 g/cc.
[5] Density for $Fe_{92}Si_8$, 7.431 g/cc.

Table 3.3 The comparison between the analytical value from the linear packing model and the actual mixture

Mixture	-45+15 μm (wt.%)	<10μm (wt.%)	Relative packing density
Packing model	67.28	32.72	67.00%[6]
Actual mixture	67	33	62.02%[6]

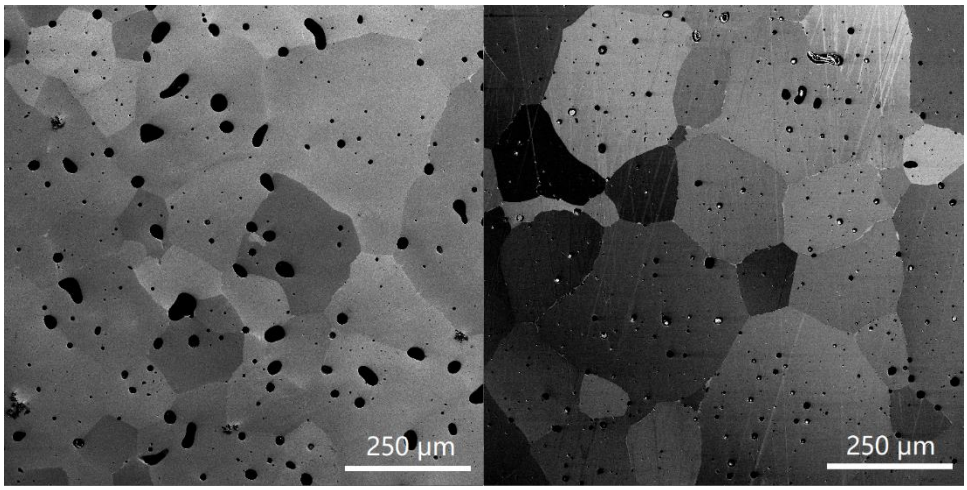

Figure 3.3 Backscatter electron image of sintered FeSi samples with different powder mixture. Left: 100 wt.% of $Fe_{92}Si_8$ alloyed powder sintered at 1300°C Right: 67 wt.% of $Fe_{92}Si_8$ + 33 wt.% of Fe powder sintered at 1250°C

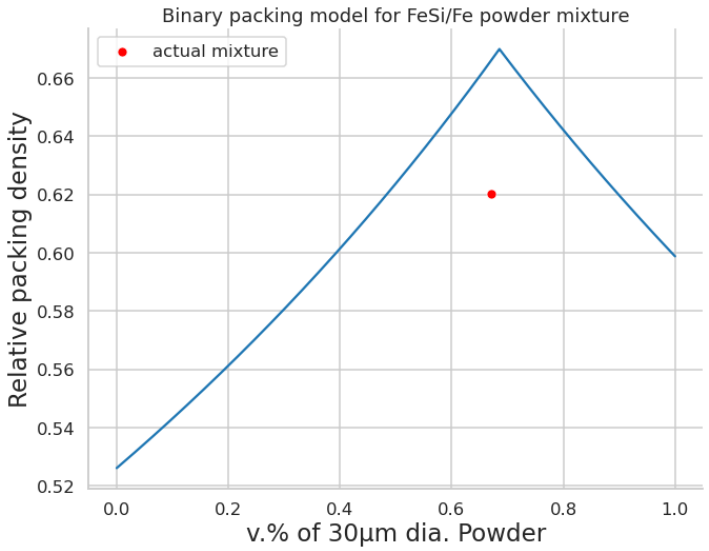

Figure 3.4 Binary powder packing model for FeSi/Fe powder, the red dot indicates the value of the actual powder mixture

[6] Estimate density for Mixed $Fe_{95}Si_5$ powder: 7.58 g/cc.

The density results of Figure 3.5 show that the alloyed density did not improve beyond 7.5 g/cc, which means that the increase in either sintering temperature or Boron content no longer improves the density. The addition of 0.25 wt.% of Boron improves the relative density by about 1~2%. Adding Boron beyond 0.5 wt.% did not increase the density. The results in Figure 3.6 show that the sample sintered at 1200°C has the highest maximum permeability with the sample sintered at 1150°C having the second-highest maximum permeability. Increasing the sintering temperature beyond 1200°C negatively impacts maximum relative permeability, reducing the value by 25%. Figure 3.7 shows that the samples sintered in lower temperatures (1150°C and 1200°C) have a lower hysteresis loss at 1.5T compared to the ones sintered in 1250°C and 1300°C. For total loss (Figure 3.8) with the frequency of 400Hz and at 0.5T, the samples with 0.25wt.% of Boron sintered at 1200°C have the lowest loss compared to other sintered temperatures.

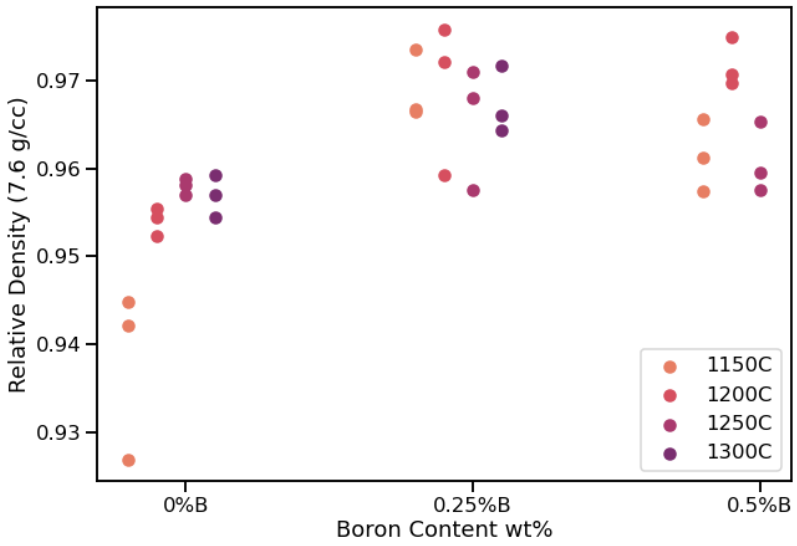

Figure 3.5 Relative density data of BJT processed $Fe_{95}Si_5$ depending on processing variables

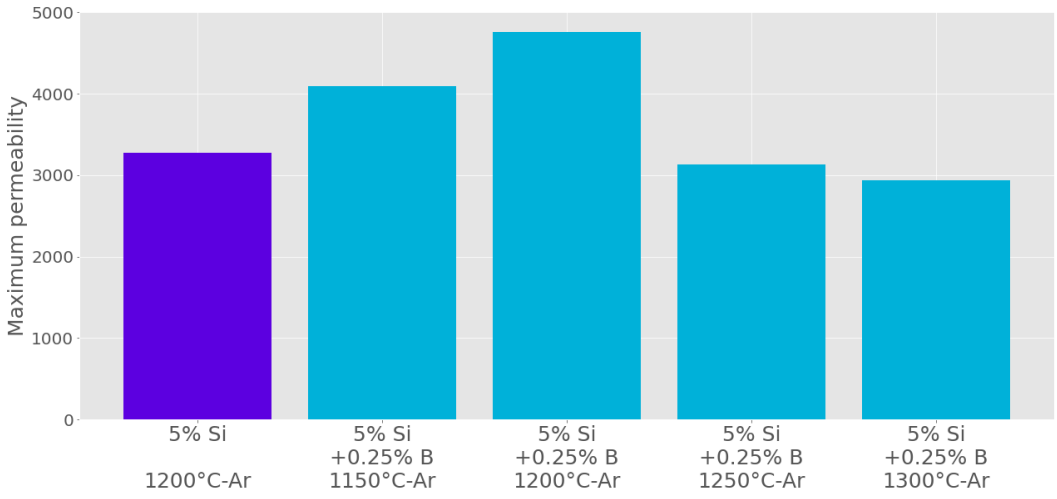

Figure 3.6 Maximum relative permeability comparison between alloyed powder mixture

The backscatter electron image shown in Figure 3.9 indicates the difference in microstructure with different Boron content from 0 to 0.5 wt.%. Without Boron, pores are present within the grains. Introducing Boron into the mixture reduces the porosity level within the grains and pores appears mostly at the grain boundaries, indicating that the additional Boron enhances the formation of liquid phase and reducing the interstitial space during the densification process.

The microstructural image of the sample with 0.5 wt.% of Boron shows that a thicker lamellar phase is formed around the grain boundary compared to the 0.25 wt.% Boron sample, indicating that the proportion of lamellar phase has a direct proportional relationship with the amount of Boron additive. The EDX analysis of the sample with 0.5 wt.% of Boron shows that the lamellar phase mainly contains Iron and Boron, meaning that the main phase at the grain boundary is either FeB or Fe_2B. The backscatter electron image for the samples with 0.25 wt.% of Boron compared based on Figure 3.10. Between the samples sintered at 1150°C and 1200°C, the change near the grain boundary is insignificant. At 1250°C, the grain boundary has a different appearance compared to the lower temperatures, where the lamellar structure seems finer compared to the samples sintered at 1150°C and1200°C. The difference at the grain boundary could be the explanation of the reduction in magnetic properties (lower permeability, higher losses) for samples sintered over 1200°C; however, further studies need to be done to draw a conclusion.

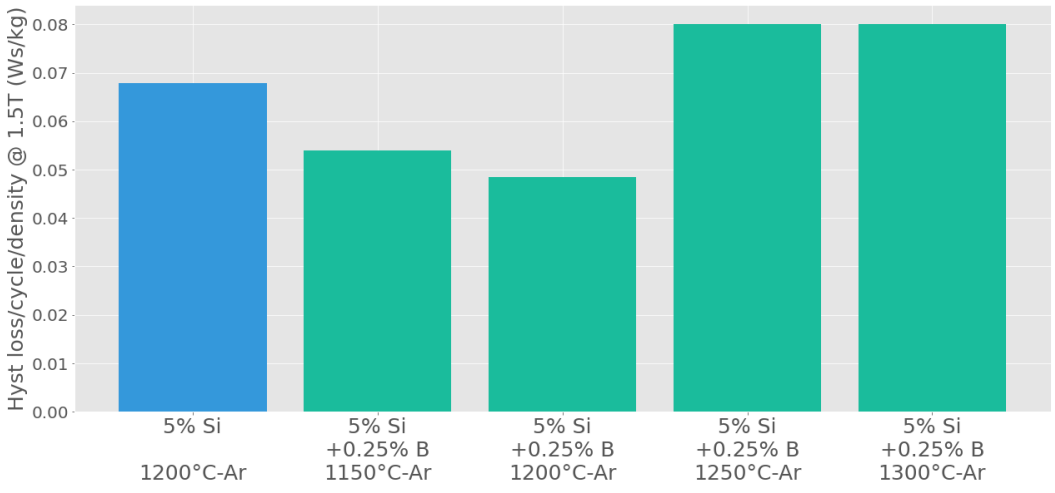

Figure 3.7 Hysteresis loss at 1.5T comparison between alloyed powder mixture

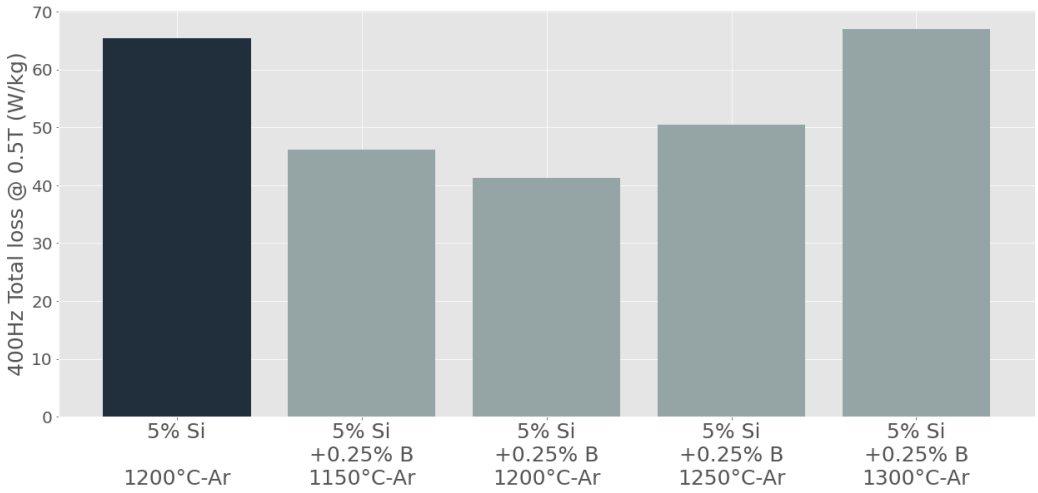

Figure 3.8 Total loss at 0.5T for 400Hz comparison between alloyed powder mixture

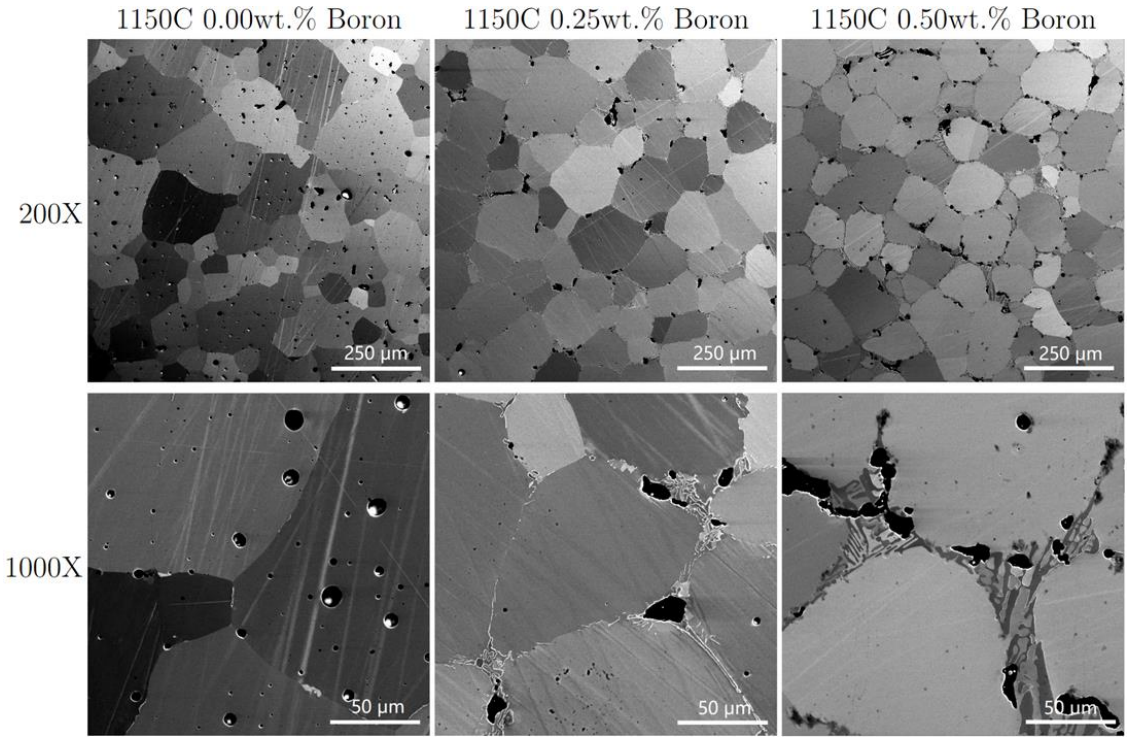

Figure 3.9 Backscatter electron image for samples sintered at 1150°C, Argon environment, with different amounts of Boron

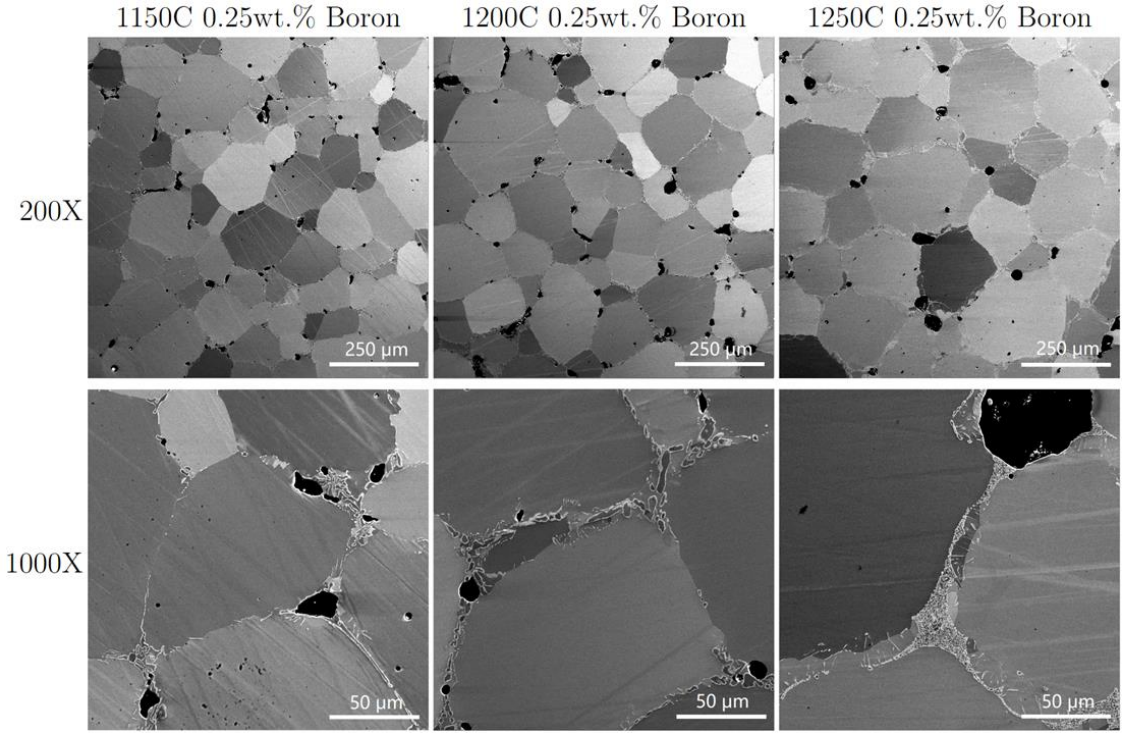

Figure 3.10 Backscatter electron image for samples with 0.25 wt.% Boron, sintered in different temperatures, Argon environment

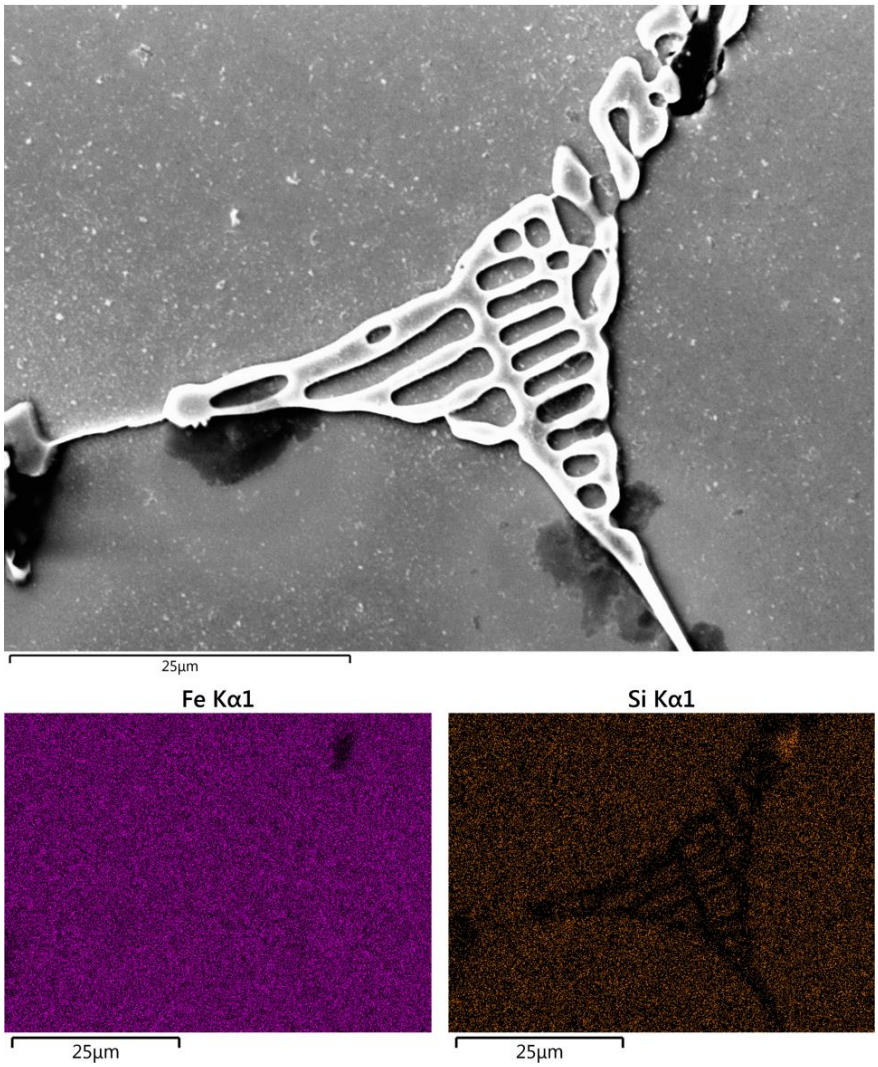

Figure 3.11 Energy dispersive X-Ray Analysis (EDX) for $Fe_{95}Si_5$ with 0.5 wt.% Boron

3.4 Application demonstration

To demonstrate the advantage of AM, a stator with designed internal cooling channels was made (Figure 3.12). The powder stock used for the stator core contains 0.25 wt.% of Boron as a sintering additive. A joining technique was used since the stator was printed in four different sections after removing the powder inside the designed cooling channels. The printed sections were assembled together and sintered using the same sintering parameters from section 3.2, mainly at 1200°C in an Argon environment for six hours. There was minor distortion during sintering as the parameters were not fully optimized. Such BJT printed stator core is unique compared to other AM approaches where complicated internal cooling channels are difficult to accomplish. For other powder-based

AM methods such as L-PBF or EBM, the separated segments of the part cannot be joined after printing. If the part is printed as one whole part, the remaining powder inside the enclosed channel cannot be removed. Currently, the stator is being mounted on the experimental setup for performance comparison.

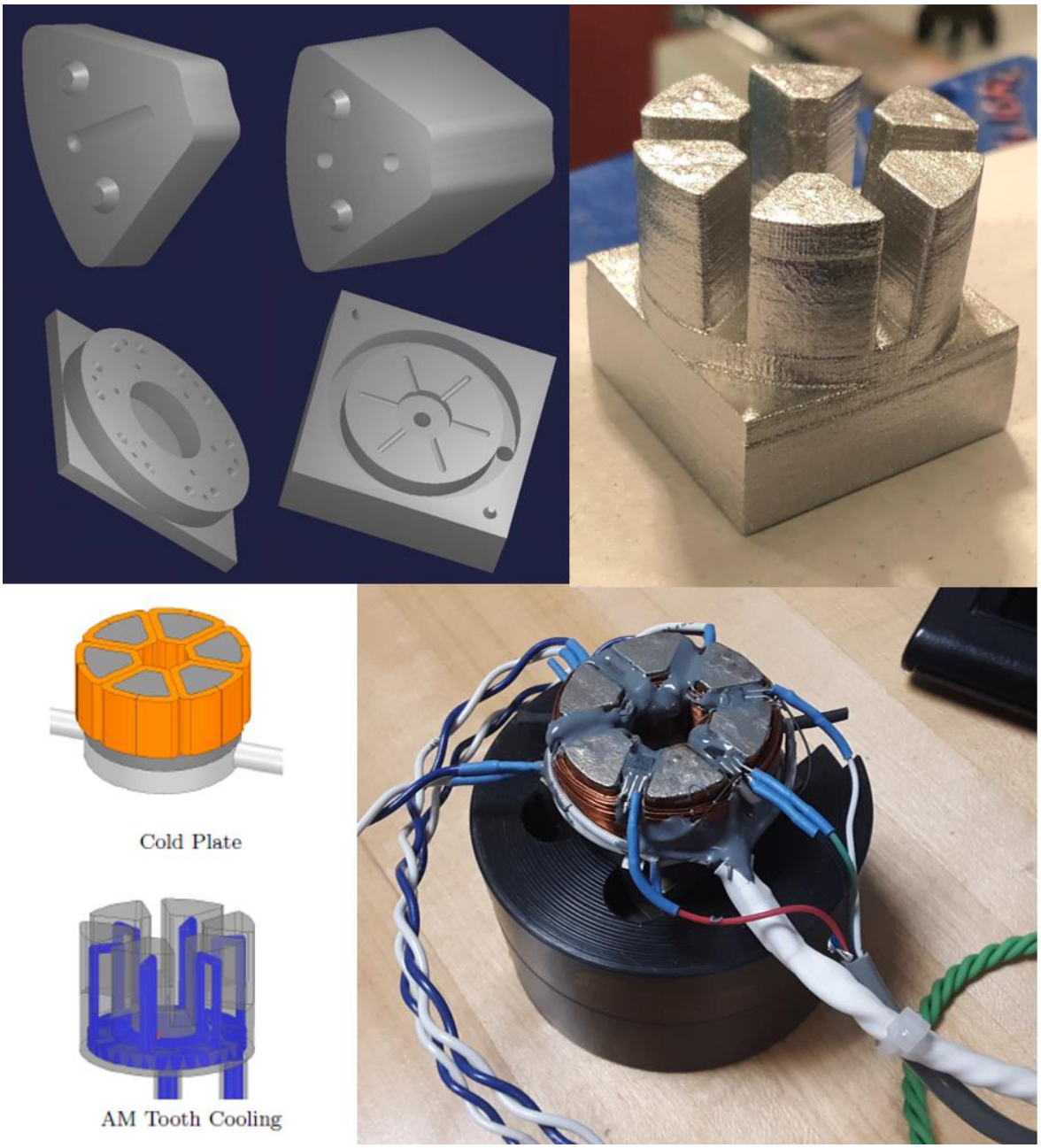

Figure 3.12 The CAD files of different parts of the stator core (top left) and the final sintered part with using the joining technique (top right). The perspective view of internal cooling channels (bottom left), an illustration of the test setup of the stator with windings (bottom right)

3.5 Discussion

Comparing the microstructure with the samples using the alloyed powder only with samples using the optimal mixing confirms the effectiveness of implementing the linear packing model. From the density measurement it shows that with 0.25 wt.% Boron addition increases the final density by 1~2% with a lower sintering temperature. From the microscopic analysis, the Boron addition is shown to be effective in closing the pores inside the grain to increase the final density. The micrograph analysis also shows that the amount of solidified liquid phase at the grain boundary is proportional to the amount of Boron additive. EDX analysis of the lamellar phase at the grain boundary as shown in Figure 3.11 shows that Iron Boride was formed. Samples with 0.25 wt.% of Boron sintered at 1200°C have the best overall property including the highest density, highest maximum relative permeability, lowest hysteresis loss, and lowest total loss at 400 Hz at 0.5T compared to other temperatures. For the sample sintered at a higher temperature (1250°C), the lamellar phase around the grain structure appears to be finer. The change of texture of the lamellar phase at the grain boundaries could be the reason that the properties of the samples sintered at 1250°C and 1300°C are worse than ones sintered at 1150°C and 1200°C. Further investigation is needed to draw a conclusion for this phenomenon. By comparing the results with the Cramer study [1], this study results a higher density, where this study achieved 7.45 g/cc compared to 7.31 g/cc with the Cramer study [1]. The total loss at the condition of 400Hz, 0.5T in this study achieved 41.24 W/kg, which is lower compared to 62.85 W/kg in Cramer et al. [1]. By comparing the tensile strength (Figure 3.13) to SMC, the BJT processed samples in this study as well as the Cramer study [1] have the main advantage because the strength is close to that of A36 structural steel. Although the ultimate tensile strength and the maximum relative permeability are lower compared to Cramer et al. [1], there is still room for improvement. Since the Silicon content used in this study was 5 wt.%, where Cramer et al. [1] used 6.5 wt.% Silicon for the optimal permeability [27], and higher Silicon content also increases the hardness of the material, which improves the tensile strength. By comparing the results between the elemental powder approach (Chapter 2) and alloyed powder approach (Chapter 3) shown in Figure 3.14, the alloyed powder approach is higher in density, higher in maximum permeability, lower in hysteresis loss, and lower in the total loss for 400Hz with 0.5T.

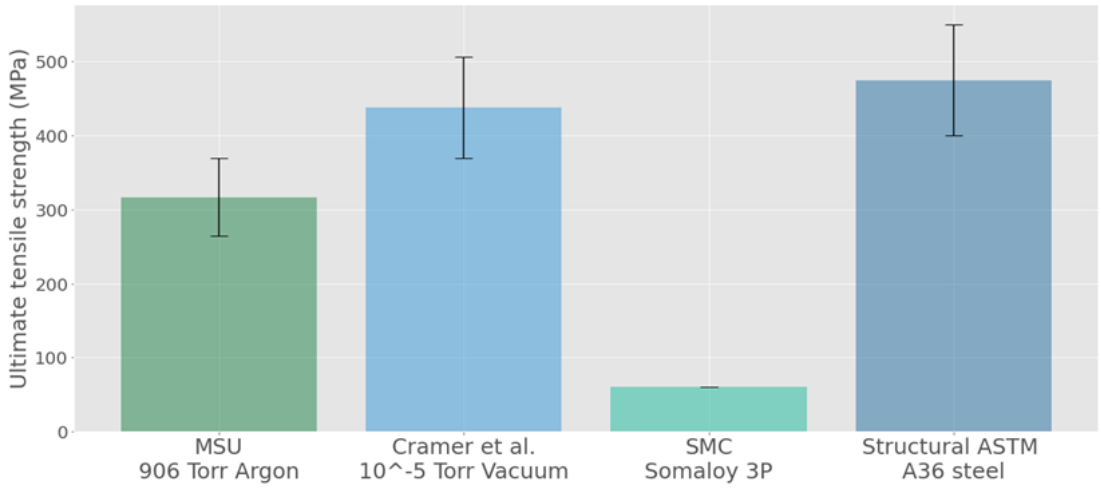

Figure 3.13 U.T.S. comparison with Cramer et al. [1], SMC Somaloy 3P [34], and ASTM A36 steel [47]

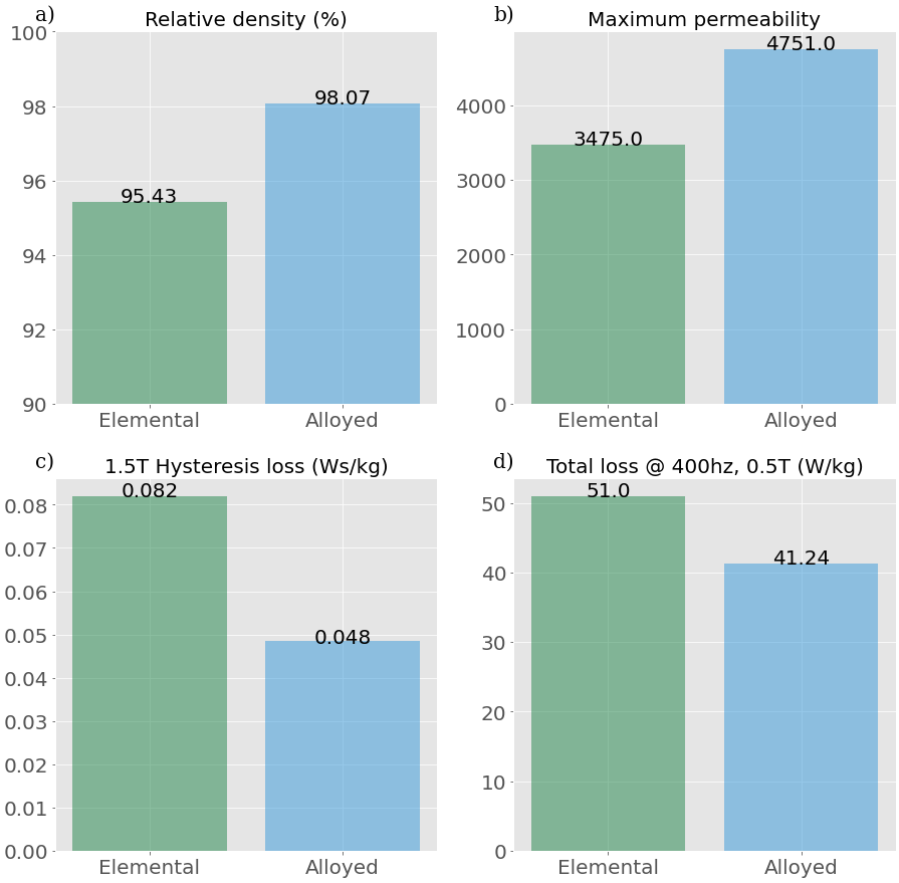

Figure 3.14 Property comparison between the elemental powder approach and the alloyed powder approach, both with the composition of $Fe_{95}Si_5$ + 0.25 wt.% 1 µm, sintered in Argon at 1200°C

CHAPTER 4 INCREASING THE SILICON CONTENT WITH ALLOYED POWDER APPROACH

4.1 Introduction

The previous two chapters investigated the possibility of fabricating high Silicon steel content using the elemental powder and alloyed powder approaches. Both of these approaches used with sintering additives to form liquid phase during the sintering process. However, both approaches only investigated the properties with the Silicon amount at 5 wt.%. Since the brittleness of increasing Silicon content is not an issue for BJT processing, there is no reason not to increase the Silicon content from 5 wt.% to 6.5 wt.%. It was reported that the 6.5 wt.% of Silicon is the optimal amount for electrical steel for permeability [27]. In this chapter, the goal is to fabricate electrical steel with the 6.5 wt.% of Silicon by adjusting the Silicon content from the base $Fe_{92}Si_8$ alloyed powder. The goal was achieved in two ways: one is by reducing the amount of smaller pure Iron powder in the mixture, and the second way is to add pure Silicon powder into the mixture used in Chapter 3.

4.2 Experimental Setup

4.2.1 Feed stock preparation

A detailed description of five different powders used in this chapter is shown in Table 4.1. The $Fe_{92}Si_8$ was used as the base powder and either the pure Iron powder or pure Silicon powder was added to adjust the Silicon level of the final powder mixture. The tapped density of the alloyed powder and the pure Iron powder were measured in Chapter 3. The powders were mixed in the high-speed mixer DAC150 from Flacktek (Landrum, SC, USA) with 1500 RPM for 100 seconds, two different powder ratios were used, one mixture by reducing the wt.% of Iron powder to adjust the Silicon content to 6.5 wt.% and the other mixture with the same optimal ratio used Chapter 3. The tapped densities of the powder mixtures were also measured and compared, and the results are presented in Table 4.2. For the other mixture, 1.2wt.% of Silicon was added later to adjust the final Silicon content to 6.5 wt.%. Two different sizes of Boron (1μm & 0.1μm) were used as additives in an attempt to control the extent of forming the liquid phase mentioned.

Table 4.1 List of powder and sintering additive materials

Element	Average powder size	Claimed purity	Company
$Fe_{92}Si_8$	30 µm	Alloyed	American Elements (CA, USA)
Fe	10 µm	≥ 99.9%	Sigma Aldrich (MO, USA)
Si	1 µm	~ 99.99%	US Research Nanomaterials (TX, USA)
B	1 µm	≥ 95%	Sigma Aldrich (MO, USA)
B	0.1 µm	~ 99.99%	US Research Nanomaterials (TX, USA)

Table 4.2 Tapped density comparison with different mixture

Mixture	$Fe_{92}Si_8$ powder	Fe powder	Predicted density	Tapped density
$Fe_{92}Si_8$	100 wt.%	0 wt.%		59.880%[7]
$Fe_{95}Si_5$	67.0 wt.%	33.0 wt.%	65.920%[8]	61.981%[2]
$Fe_{93.5}Si_{6.5}$	82.3 wt.%	17.7 wt.%	62.080%[9]	58.075%[3]

4.2.2 Sample preparation

X1-Lab from ExOne (North Huntington, PA, USA) was used to print the rings with the dimension of 38 mm outer diameter, 30 mm inner diameter and 4 mm height to measure the magnetic properties and cubes with 8 mm edge length for cross-sectional analysis. The detailed printing process is already described in Chapter 1, Section 1.3.1. The printing parameter for the samples was set at 2.1:1 powder feed ratio, the layer thickness is set to 100 µm. The saturation rate is set to 70%, with the powder packing rate set to 60%. The initial rolling speed is set to 0.3 mm per second. The printed parts are placed in an air furnace at 195°C for 2 hours for curing. For sintering in an Argon environment, the samples were placed in a carbon lined resistance furnace MRF T-16X26-G-G-3000-VM-G (Material research furnaces, Allenstown, NH). The chamber is prepared by vacuuming and refilling the chamber with ultra-high purity Argon (~99.999%), the purging cycle is repeated three times to reduce oxygen content in the chamber. For vacuum environment sintering, the samples were placed in a molybdenum lined resistance furnace manufactured by T-M Vacuum

[7] Estimated density for $Fe_{92}Si_8$: 7.43048 g/cc.
[8] Estimated density for $Fe_{95}Si_5$: 7.58129 g/cc.
[9] Estimated density for $Fe_{93.5}Si_{6.5}$: 7.50900 g/cc.

products Inc. (Cinnaminson, NJ). The chamber pressure is pumped down to ~10^{-2} Torr and continuously pumped during the sintering process. After the chamber preparation, the samples were heated at a 5°C/min ramp rate to the set temperature and dwelled for 6 hours, then cooled to room temperature 15°C/min. The densities of the samples were then measured by Archimedes method with ~99.5% isopropanol alcohol. The ring samples were measured for magnetic characterization. The cube samples are sectioned, mounted, and polished for the cross-section analysis.

4.2.3 Sample characterization

For magnetic characterization, the procedure is the same as described in Chapter 2, Section 2.3.4.3. For preparing cross-section analysis for the samples, the cube samples were cut, mounted, and mechanically polished using a series of 240, 400, 600, and 1200 US grit size SiC abrasive papers then followed by alumina suspension with the particle size 1 μm and 0.3 μm. The final polishing was then performed using a colloidal silica solution (0.06 μm crystallite size). A JEOL 6610 scanning electron microscope was used for back scattering electron imaging, the energy level was set to 20kV with the working distance of 10 mm. The x-ray diffraction (XRD) was performed by Rigaku Ultima IV system with a copper anode target (1.54 Å) with 40 kV acerating voltage and the beam intensity of 44 mA in Bragg Brentano configuration, 0.01° step size was used within the range of $10° < 2\theta < 150°$. The data were collected and analyzed using Rigaku software. ImageJ software was used for the cross-sectional analysis for estimating the percentage of dark regions from the back scattering electron images.

4.3 Results

From the tapping density result, the mixtures with the reduced amount of smaller powder yielded lower tapped density compared to the tapped density of the alloyed base powder. The reason of this phenomena is because the van der Waals force has a relatively more significant effect for smaller particles [48], the powder will repel against each other, making the final mixture less packed. Hence, the approach to increasing the final Silicon content by reducing the amount of smaller Iron powders is no longer suitable. Samples using the optimal mixing ratio with additional Silicon are further analyzed and compared.

For the samples with additional Silicon only, with the sintering temperature increased by 150°C, the density only was increased by about 0.5% (Figure 4.1), indicating that Silicon as an additive is not as effective as Boron to improve the final density.

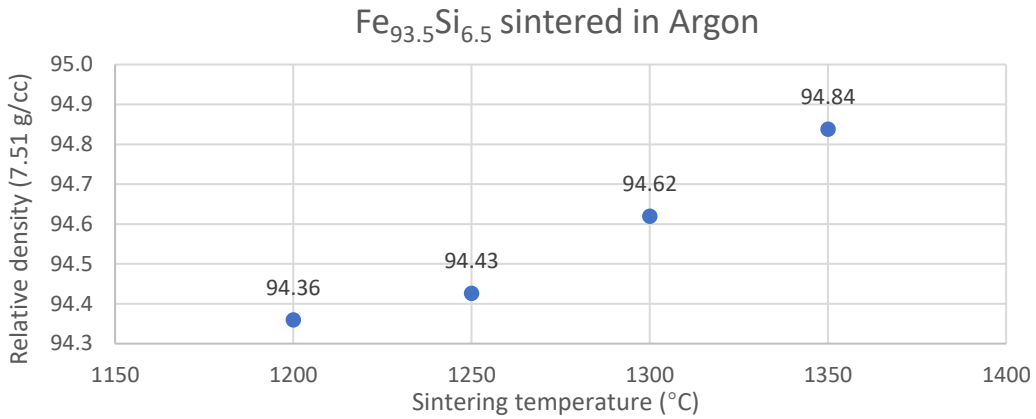

Figure 4.1 Relative density of $Fe_{93.5}Si_{6.5}$ sintered in Argon environment at different temperatures

The density improvement with Boron additive is more significant than with Silicon additive. With Boron additive, the sintered parts reach the relative density of 97.3% at 1150°C, reaching the maximum density at 1150°C. The 0.25 wt.% Boron still has a significant effect on improving the final density of the samples.

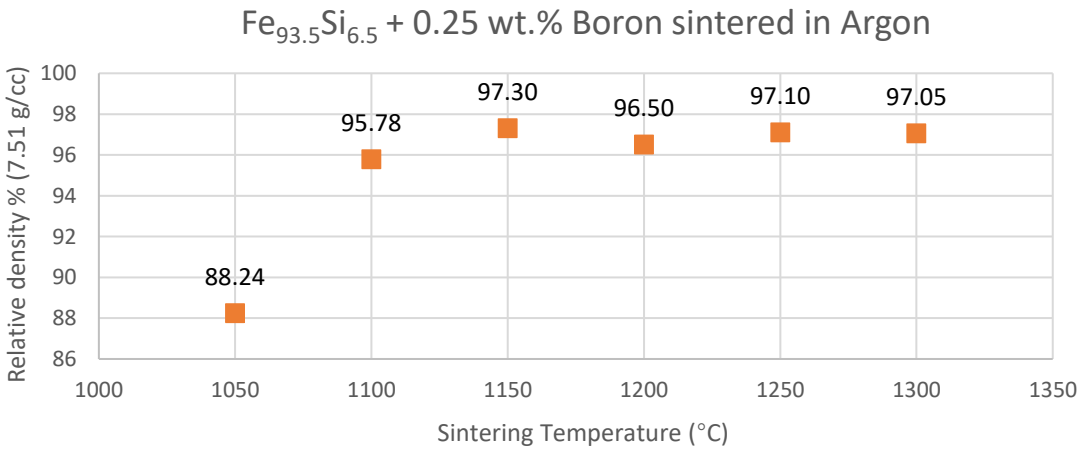

Figure 4.2 Relative density of $Fe_{93.5}Si_{6.5}$ with Boron additive sintered in Argon environment at different temperatures

Additional Silicon samples and the mixture used in Chapter 3 ($Fe_{95}Si_5$ + 0.25 wt.% 1 μm Boron) were compared with XRD analysis (Figure 4.3). Both compositions result in the exact same peaks,

indicating that additional Silicon did not change the phases in the materials. By comparing the properties of the samples in Figure 4.6, to the same size of Boron additive, the increase in the Silicon content decreases the relative density by 1.30%, increases the maximum permeability by 65.74%, increases the hysteresis loss by 18.49%, and decreases in the total loss at 400 Hz, 0.5T by 29.30%. The increase in the maximum permeability was expected since 6.5 wt.% Silicon is the optimal amount for maximum permeability [27]. The impact on the density and hysteresis loss due to the increase in the Silicon content can be further investigated from the micrograph (Figure 4.6 A & B). The image analysis showed that the area percentage of the dark region for 6.5 wt.% Silicon is higher than 5 wt.% Silicon. The irregular porosity shows that the additional Silicon is blocking the liquid phase to fill in the interstitial between powders, leading to irregular grain shapes, which explains the reason for the higher hysteresis loss [49]. Similar porosity pattern was not shown in the samples with the large Boron additive only (Figure 4.6 A).

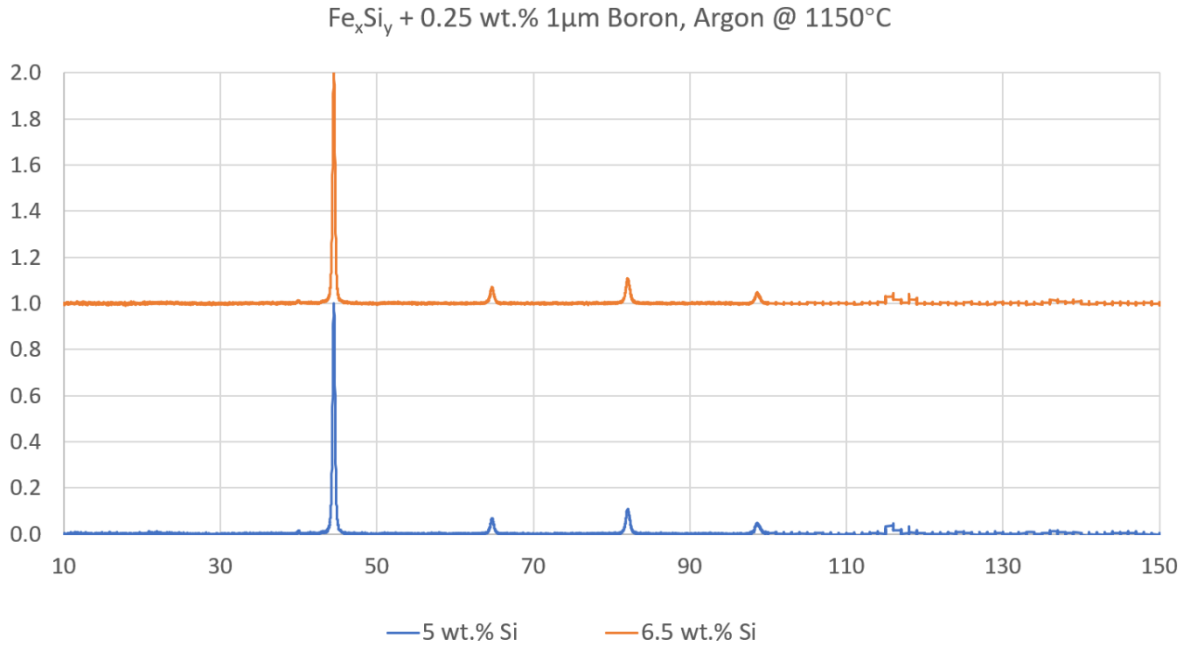

Figure 4.3 XRD comparison with different Silicon content samples sintered in Argon environment at 1150°C within the range of 10°C < 2θ < 150°C

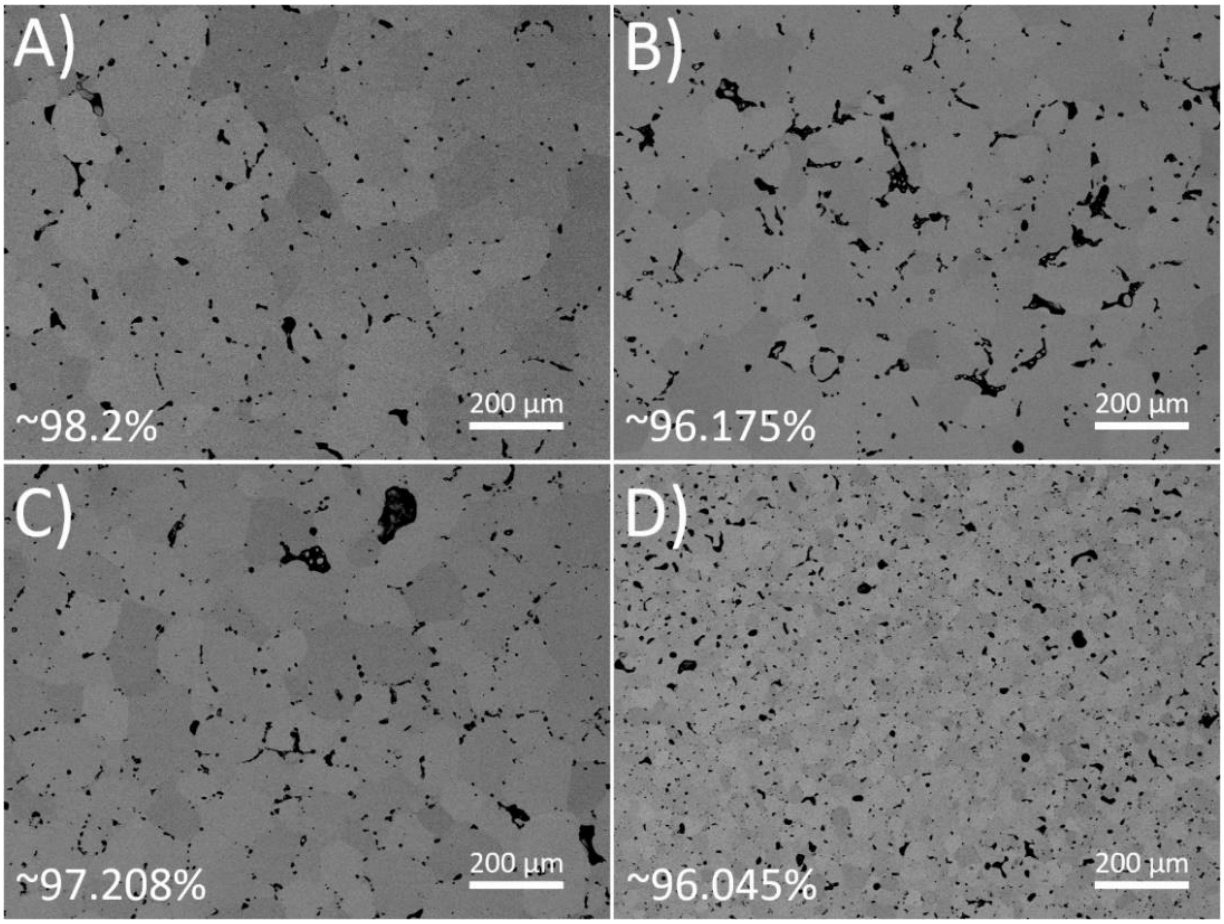

Figure 4.4 Back scattering electron image for FeSi samples sintered at 1150°C. The percentage density processed by ImageJ is shown on the bottom left corner
A) $Fe_{95}Si_5$ + 0.25 wt.% Boron (1 µm) sintered in Argon
B) $Fe_{93.5}Si_{6.5}$ + 0.25 wt.% Boron (1 µm) sintered in Argon
C) $Fe_{93.5}Si_{6.5}$ + 0.25 wt.% Boron (0.1 µm) sintered in Argon
D) $Fe_{93.5}Si_{6.5}$ + 0.25 wt.% Boron (0.1 µm) sintered in vacuum

The impact of reducing the size of the Boron additive was shown in Figure 4.6. The density was increased by about 1.92%, which corroborated with the micrograph. The maximum permeability increased by about 4.75% and the hysteresis loss was reduced by about 20.339%. The micrograph (Figure 4.4 B & C) shows that the pores are less irregular for the smaller size Boron compared to the larger ones. Since smaller size Boron can be distributed more evenly around the larger powders, it allows less localized liquid phase formation, which resolves the irregular porosity caused by additional Silicon, making the grain shape less deformed, which reduces the hysteresis loss as a result [49]. The total loss is similar between two additive sizes. The slightly higher eddy current loss is led by higher density.

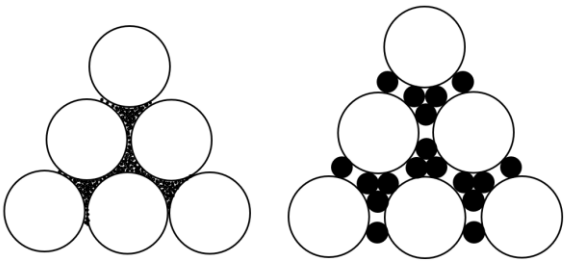

Figure 4.5 A schematic to illustrate the reduction in the size of sintering additive can be more well-distributed around the base powders

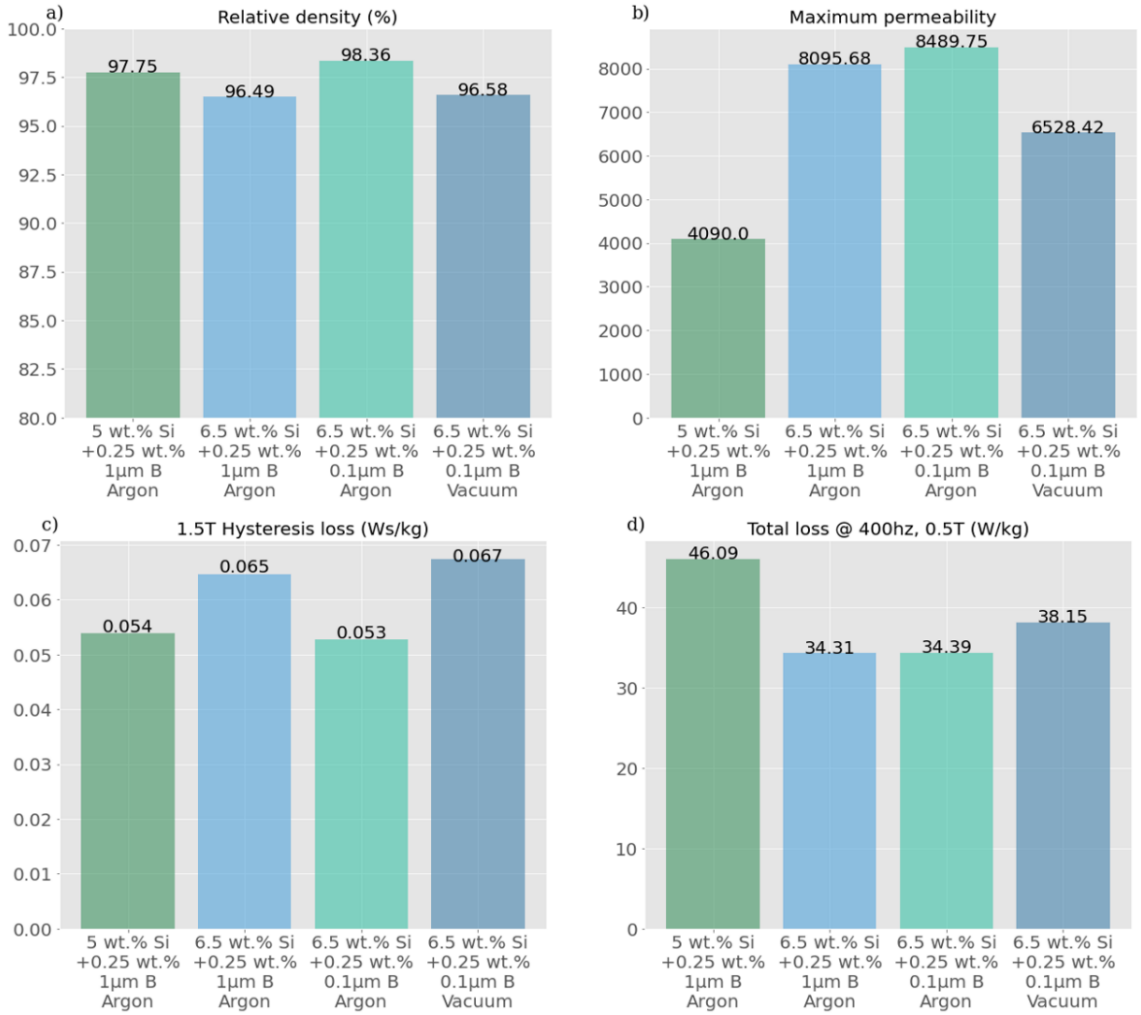

Figure 4.6 Properties comparison for different condition changes (from left to right): Increasing Silicon content (5 wt.% → 6.5 wt.%), change in Boron size (1 µm → 0.1 µm), & change in sintering environment (Argon → Vacuum). a) Density b) Maximum permeability c) Hysteresis loss at 1.5T d) Total loss at 400Hz, 0.5T

Since a vacuum environment promotes material transport in liquid phase sintering [50], the effect of sintering in a vacuum environment is compared. By changing the sintering environment to vacuum, Figure 4.6 shows that, for the same composition with the same 0.1 μm size Boron sintered at 1150°C, all the properties are worse for the vacuum environment. The density and permeability are lower, and the hysteresis loss and total loss are higher. The micrograph (Figure 4.4 D) shows that the grain structure of the sample sintered in vacuum. This is evident as the sintering environment does have an impact on the grain growth when sintering Silicon steel with additional Boron. This could explain the reason for the vacuum environment influencing the grain formation, since the reduction in pressure changes the eutectic point among Iron Silicon and Boron [51, 52], creating worse results in all the properties (lower in density, lower in maximum relative permeability, higher in losses) compared to the samples sintered in Argon. Further investigation needs to be done to explain this phenomenon.

4.4 Conclusion

By adding Silicon sintering additive, the relative density only increases by 0.5% from 1200°C to 1350°C. With an additional 0.25 wt.% of Boron, the maximum relative density was increased by 2% when sintering at 1150°C. By comparing the powder mixture used in Chapter 3 ($Fe_{95}Si_5$ + 0.25 wt.% Boron), the maximum permeability was increased by about 65.74%; the total loss was decreased by 29.30%. The Silicon additive blocks the liquid phase to fill interstitials between powders, leading the material with irregular shape pores resulting in the material with a lower density and a higher hysteresis loss. The issue can be resolved by using a smaller size Boron to evenly distribute the liquid phase formation, resulting in the maximum relative permeability. The relative density is the highest among all four combinations (8489.75 and 98.36% respectively) and the lowest in hysteresis loss at 1.5T for 0.053 Ws/kg. The total loss was increased by higher density, but the amount was insignificant (0.23%), resulting in a value of 34.39 W/kg at 400Hz, 0.5T. Changing the sintering environment from Argon to vacuum changed the microstructure of the material, resulting in a reduction in density, maximum permeability, increase in hysteresis loss and total loss. The relationship between the microstructure and the sintering pressure of the Fe-Si-B system needs to be investigated in a future study. Comparing the results to Cramer's paper [1] the approach in this chapter results a 1.09% increase in relative density, 58.54% decrease in total loss

at 400Hz with 0.5T induction even though the maximum permeability is reduced by 23%. However, there is room for improvements by using different post processing techniques, such as annealing the hydrogen environment, which can decarburize the material [53], further reducing the hysteresis loss [27].

4.5 Future works

Since this study does not incorporate a binder burnout process for the green parts, the residual carbon content may introduce impurities, that could influence the hysteresis loss, according to Figure 4.7. Additionally, during the binder curing process, oxidation might occur with the pure Iron powders present in the mixture. This could lead to an excessive oxygen content, further impacting the hysteresis loss (Figure 4.7). Therefore, various post-processing methods must be investigated. For instance, annealing in a hydrogen atmosphere could be explored to reduce oxide content, or performing the process in a carbon monoxide environment could be considered for decarburization [54]. Furthermore, from Figure 4.7, phosphorus could be a candidate as an additive into the matrix for reducing hysteresis loss.

Aside from the axial flux motor designed and built in chapter 3, a transvers flux motor (TFM) design can also be considered for its high torque density and efficiency. The key distinguishing feature of a TFM is its unique magnetic circuit design, where the magnetic flux is perpendicular (transversely) to the rotor's movement. Due to the nature of their complex structure of the design, such as some examples shown in Figure 4.8, TFM could greatly benefit from the precision and flexibility offered by additive manufacturing methods.

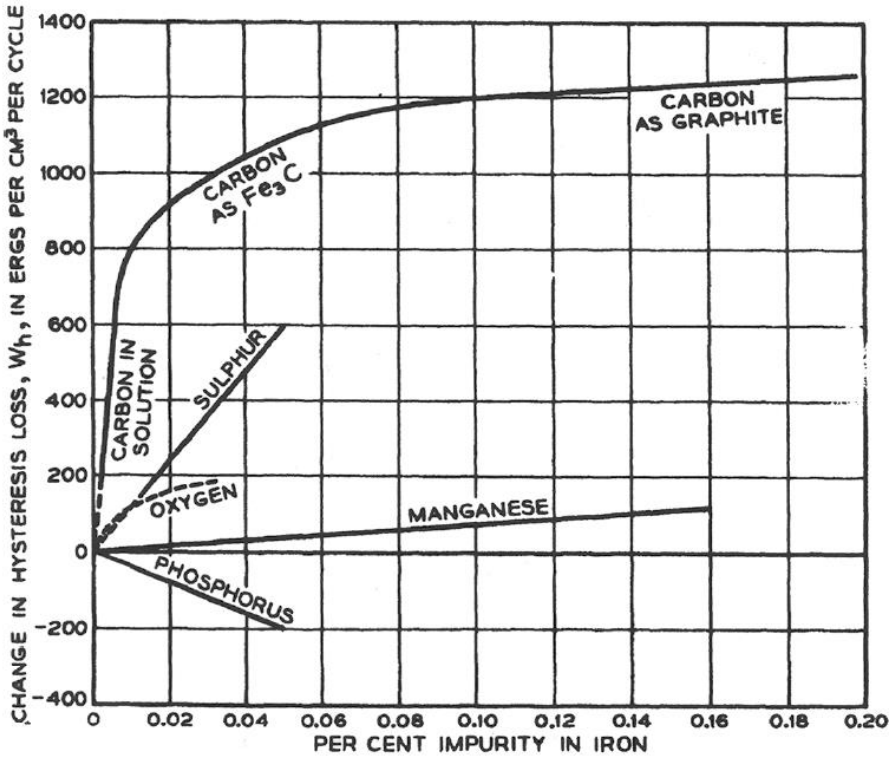

Figure 4.7 The effect of different impurities on the hysteresis losses of $Fe_{96}Si_4$ at B = 10000 [27]

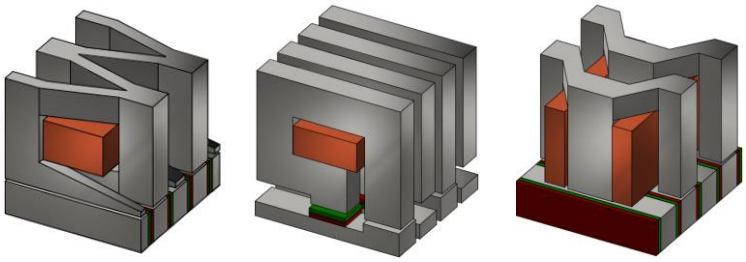

Figure 4.8 Few examples of a segment of the core structure with coil (colored in copper) magnets (green/red), and soft magnetic material(gray) of main flux path [55]

BIBLIOGRAPHY

[1] C. Cramer, P. Nandwana, J. Yan, S. Evans, A. Elliott, C. Chinnasamy and M. Paranthaman, "Binder jet additive manufacturing method to fabricate near net shape crack-free highly dense FE-6.5 wt.% Si Soft magnets," *Heliyon,* vol. 5, no. 11, 2019.

[2] J. F. Gottwald, "Liquid metal recorder". United States of America Patent US3596285A, 11 July 1969.

[3] *Additive manufacturing — General principles — Fundamentals and vocabulary,* ISO/ASTM 52900:2021(en), 2021.

[4] "Material Extrusion," ACAM Aachen Center for Additive Manufacturing, 27 May 2020. [Online]. Available: https://acam.rwth-campus.com/material-extrusion_mit-rahmen/.

[5] H. X. Nguyen, H. Suen, B. Poudel, P. Kwon and H. Chung, "Development of an innovative, high speed, large-scaled, and affordable metal additive manufacturing process," *CIRP Annals,* vol. 69, no. 1, pp. 177-180, 2020.

[6] S. Sing, C. Tey, J. Tan, S. Huang and W. Y. Yeong, "3D printing of metals in rapid prototyping of biomaterials: Techniques in additive manufacturing," in *Rapid Prototyping of Biomaterials*, R. Narayan, Ed., Woodhead Publishing, 2020, pp. 17-40.

[7] C. Zhang, F. Chen, Z. Huang, M. Jia, G. Chen, Y. Ye, Y. Lin, W. Liu, B. Chen, Q. Shen, L. Zhang and E. J. Lavernia, "Additive manufacturing of functionally graded materials: A review," *Materials Science and Engineering: A,* vol. 764, p. 138209, 2019.

[8] "How to design parts for material jetting in 3D printing," HUBS, [Online]. Available: https://www.hubs.com/knowledge-base/how-design-parts-material-jetting-3d-printing/. [Accessed 17 May 2023].

[9] A. P., "The Complete Guide to Material Jetting (PolyJet) in 3D Printing," 3Dnatives, 25 July 2019. [Online]. Available: https://www.3dnatives.com/en/polyjet100420174/#!. [Accessed 17 May 2023].

[10] A. Hehr and M. Norfolk, "A comprehensive review of ultrasonic additive manufacturing," *Rapid Prototyping Journal,* vol. 26, no. 3, pp. 445-458, 2019.

[11] *UAM Mini Heat Exchanger and Dissimilar Metal Examples,* Fabrisonic LCC, 2016.

[12] S. Sun, M. Brandt and M. Easton, "Powder bed fusion processes: An overview," *Laser Additive Manufacturing,* pp. 55-77, 2017.

[13] T. Do, P. Kwon and C. S. Shin, "Process development toward full-density stainless steel parts with binder jetting printing," *International Journal of Machine Tools and Manufacture,* vol. 121, pp. 50-60, 2017.

[14] S. Mirzababaei, B. K. Paul and S. Pasebani, "Metal Powder Recyclability in Binder Jet Additive Manufacturing," *Journal of the Minerals, Metals & Materials Society,* vol. 72, no. 9, pp. 3070-3079, 06 July 2020.

[15] J. L. Bartlett and X. Li, "An overview of residual stresses in metal powder bed fusion," *Additive Manufacturing,* vol. 27, pp. 131-149, 2019.

[16] C. Li, Z. Liu, X. Fang and Y. Guo, "Residual Stress in Metal Additive Manufacturing," *Procedia CIRP,* vol. 71, pp. 348-353, 2018.

[17] Y. Tang, Z. Huang, j. Yang and Y. Xie, "Enhancing the Capillary Force of Binder-Jetting Printing Ti6Al4V and Mechanical Properties under High Temperature Sintering by Mixing Fine Powder," *Metals,* vol. 10, no. 10, 2020.

[18] R. M. German, Liquid Phase Sintering, New York, NY: Springer, 1985.

[19] T. Stovall, F. de Larrard and M. Buil, "Linear packing density model of grain mixtures," *Powder Technology,* vol. 48, no. 1, pp. 1-12, 1986.

[20] R. M. German, P. Suri and S. J. Park, "Review: liquid phase sintering," *Journal of Materials Science,* vol. 44, no. 1, pp. 1-39, 2009.

[21] S. Lu, G. Meenashisundaram, P. Wang, S. Nai and J. Wei, "The combined influence of elevated pre-sintering and subsequent bronze infiltration on the microstructures and mechanical properties of 420 stainless steel additively manufactured via binder jet printing," *Additive Manufacturing,* vol. 34, 2020.

[22] L. Haferkamp, L. Haudenschild, A. Spierings, K. Wegener, K. Riener, S. Ziegelmeier and G. J. Leichtfried, "The Influence of Particle Shape, Powder Flowability, and Powder Layer Density on Part Density in Laser Powder Bed Fusion," *Metals,* vol. 11, no. 3, p. 418, 2021.

[23] R. K. Enneti and K. C. Prough, "Effect of binder saturation and powder layer thickness on the green strength of the binder jet 3D printing (BJ3DP) WC-12%Co powders," *International Journal of Refractory Metals and Hard Materials,* vol. 84, 2019.

[24] X. Ye, Y. Li, Y. Ai and Y. Nie, "Novel powder packing theory with bimodal particle size distribution-application in superalloy," *Advanced Powder Technology,* vol. 29, no. 9, pp. 2280-2287, 2018.

[25] W. Du, X. Ren, Y. Chen, C. Ma, M. Radovic and Z. Pei, "Model Guided Mixing of Ceramic Powders With Graded Particle Sizes in Binder Jetting Additive Manufacturing," in *ASME 2018 13th International Manufacturing Science and Engineering Conference*, College Station, Texas, USA, 2018.

[26] *Standard Test Method for Tap Density of Metal Powders and Compounds,* ASTM B527-22, 2023.

[27] R. M. Bozorth, Ferromagnetism, Wiley-IEEE Press, 1978.

[28] G. Ouyang, X. Chen, Y. Liang, C. Macziewski and J. Cui, "Review of Fe-6.5 wt%Si high silicon steel—A promising soft magnetic material for sub-kHz application," *Journal of Magnetism and Magnetic Materials,* vol. 481, pp. 234-250, 2019.

[29] Y. Wang, Y.-B. Xu, Y.-X. Zhang, F. Fang, X. Lu, H.-T. Liu and G.-D. Wang, "Development of microstructure and texture in strip casting grain oriented Silicon Steel," *Journal of Magnetism and Magnetic Materials,* vol. 379, pp. 161-166, 2015.

[30] D. S. Petrovič, B. Arh, F. Tehovnik and M. Pirnat, "Magnesium Non-metallic Inclusions in Non-oriented Electrical Steel Sheets," *ISIJ International,* vol. 51, no. 12, pp. 2069-2075, 2011.

[31] "MAGNETIC PROPERTIES," MICRO NDT SOLUTIONS & TRAINING INSTITUTE, 23 August 2019. [Online]. Available: https://microndt.com/2019/09/14/magnetic-properties/. [Accessed 17 May 2023].

[32] *Standard Classification of Insulating Coatings by Composition, Relative Insulating Ability and Application,* ASTM A976-18, 2018.

[33] T. Ros-Yáñez, D. Ruiz, J. Barros and Y. Houbaert, "Advances in the production of high-silicon electrical steel by thermomechanical processing and by immersion and diffusion annealing," *Journal of Alloys and Compounds,* vol. 369, no. 1-2, pp. 125-130, 2004.

[34] "Somaloy 3P material data," Höganäs, 2018.

[35] T. Q. Pham, H. Suen, P. Kwon and S. N. Foster, "Characterization of Magnetic Anisotropy for Binder Jet Printed Fe93.25Si6.75," in *2019 IEEE Energy Conversion Congress and Exposition (ECCE)*, Baltimore, MD, USA, 2019.

[36] M. Garibaldi, I. Ashcroft, N. Hillier, S. Harmon and R. Hague, "Relationship between laser energy input, microstructures and magnetic properties of selective laser melted Fe-6.9%wt Si soft magnets," *Materials Characterization,* vol. 143, pp. 144-151, 2018.

[37] K. J. Jhong, W.-C. Huang and W. H. Lee, "Microstructure and Magnetic Properties of Magnetic Material Fabricated by Selective Laser Melting," *Physics Procedia,* vol. 83, pp. 818-824, 2016.

[38] D. Goll, D. Schuller, G. Martinek, T. Kunert, J. Schurr, C. Sinz, T. Schubert, T. Bernthaler, H. Riegel and G. Schneider, "Additive manufacturing of soft magnetic materials and components," *Additive Manufacturing,* vol. 27, pp. 428-439, 2019.

[39] O. K. Goldbeck, IRON—Binary Phase Diagrams, Heidelberg: Springer Berlin, 1982.

[40] *Standard Test Method for Direct Current Magnetic Properties of Low Coercivity Magnetic Materials Using Hysteresigraphs,* ASTM A773/A773M-21, 2021.

[41] *Standard Test Method for Alternating-Current Magnetic Properties of Toroidal Core Specimens Using the Voltmeter-Ammeter-Wattmeter Method,* ASTM A927/A927M-18, 2022.

[42] G. Kumari, T. Q. Pham, H. Suen, T. Rahman, P. Kwon, S. N. Foster and C. J. Boehlart, "Improving the soft magnetic properties of binder jet printed iron-silicon alloy through boron addition," *Materials Chemistry and Physics,* vol. 296, p. 127181, 2023.

[43] *Standard Test Methods for Determining Average Grain Size,* ASTM E112-13, 2021.

[44] D. N. Yoon and W. J. Huppmann, "Grain growth and densification during liquid phase sintering of W-Ni," *Acta Metallurgica,* vol. 27, no. 4, pp. 693-698, 1979.

[45] T. Q. Pham, H. Suen, P. Kwon, G. Kumari, C. J. Boehlert and S. N. Foster, "Reduction in Hysteresis Loss of Binder Jet Printed Iron Silicon With Boron," *IEEE Transactions on Industry Applications ,* vol. 57, no. 5, pp. 4864 - 4873, 2021.

[46] *Standard Tension Testing of Metallic Materials,* ASTM E8 E8M-13a, 2013.

[47] AISC, Steel Construction Manual 15th Ed., AMERICAN INSTITUTE OF PHYSICS , 2017.

[48] J. Q. Feng and D. A. Hays, "Relative importance of electrostatic forces on powder particles," *Powder Technology,* Vols. 135-136, pp. 65-75, 2003.

[49] F. Landgraf, M. Emura, J. Teixeira and M. de Campos, "Effect of grain size, deformation, aging and anisotropy on hysteresis loss of electrical steels," *Journal of Magnetism and Magnetic Materials,* Vols. 215-216, pp. 97-99, 2000.

[50] V. Minin, "Effects of vacuum on the sintering and properties of a ferrite," *Soviet Powder Metallurgy and Metal Ceramics,* vol. 17, pp. 40-46, 1978.

[51] K. Nagaoka, T. Makita, N. Nishiguchi and M. Moritoki, "Effect of pressure on the solid-liquid phase equilibria of binary organic systems," *International Journal of Thermophysics ,* vol. 10, pp. 27-34, 1989.

[52] H. Wang, R. Liu, M. Ma, M. Gao, Y. Yao and W. Wang, "Solidification of FeSi2 alloy under high pressure," *Acta Physica Sinica - Chinese Edition,* vol. 53, no. 7, pp. 2378-2383, 2004.

[53] A. Zhornyak and V. Oliker, "Reduction and decarburization during the annealing of atomized iron-carbon alloy powders," *Soviet Powder Metallurgy and Metal Ceramics volume,* vol. 21, pp. 84-93, 1982.

[54] A. Zhornyak and V. Oliker, "Reduction and decarburization during the annealing of atomized iron-carbon alloy powders," *Soviet Powder Metallurgy and Metal Ceramics,* vol. 21, pp. 84-93, 1982.

[55] B. Kaiser and N. Parspour, "Transverse Flux Machine—A Review," *IEEE Access,* vol. 10, pp. 18395-18419, 2022.

APPENDIX

The PYTHON language is used to implement the linear packing model for predicting the optimal packing ratio for different size powders. The following attachments are the sample codes used in this study.

```
import matplotlib.pyplot as plt
import matplotlib
import numpy as np
import math
import pandas as pd
import seaborn as sns
import sys
import random
%matplotlib inline

def powder_packing(beta,d,r):
    import numpy as np
    import ternary

    beta = np.array(beta)
    Gamma_i = []
    y_sol  = []
    Sum1 = 0
    Sum2 = 0
    d = np.array(d)*10E-6
    n = len(d)
    s = 1
    resolution = 1/r

    vol_frac = np.arange(0,1+resolution,resolution)
```

```
    for y1 in vol_frac:
        y2 = 1-y1
        #normalization
        y = [y1, y2]
        Gamma_i_temp = []
        for i in range(n):

            Sum1 = 0
            Sum2 = 0

            for j in range(0,i):
                b = 1-(1-d[i]/d[j])**1.5
                Sum1 += (1 - beta[i]+b*beta[i]*(1-1/beta[j]))*y[j]
            for j in range(i+1,n):
                a = (1-(1-d[j]/d[i])**1.02)**0.5
                Sum2 += (1 - a*beta[i]/beta[j])*y[j]



            Gamma_i_temp.append(beta[i]/(1 - Sum1 - Sum2))

        Gamma_i.append(min(Gamma_i_temp))
        y_sol.append([y1, y2,min(Gamma_i_temp)])
    return np.array(y_sol[np.argmax(Gamma_i)]),np.array(y_sol)

#relative density
beta = [0.598804, 0.526112]
#average diameter
d = [30, 10]
#resolution
r = 10000
y = powder_packing(beta,d,r)
```

```
y_sol_max = y[0]
y_sol = y[1]

y_sol_df = pd.DataFrame(y_sol, columns = ["v% of {}um dia. Powder".format(d[0]),
                                          "v% of {}um dia. Powder".format(d[1]),
                                          "relative packing density"])

y_sol_actuall_mix_df = pd.DataFrame([[0.67,0.33,0.62018]], columns = ["v% of {}um dia.
Powder".format(d[0]),
                                                                      "v% of {}um dia. Powder".format(d[1]),
                                                                      "relative packing density"])

sns.set_style("whitegrid")
sns.set_context("talk")
sns.relplot(data=y_sol_df,
            x="v% of {}um dia. Powder".format(d[0]),
            y="relative packing density",
           estimator = None,
           kind = "line",
           height=7,
           aspect=4/3)
sns.scatterplot(data = y_sol_actuall_mix_df ,x ="v% of {}um dia. Powder".format(d[0]),y =
"relative packing density", color = "red", label = "actual mixture")

plt.xlabel('v.% of {}um dia. Powder' .format(d[0]), fontsize = 23)
plt.ylabel('Relative packing density', fontsize = 23)
plt.title('Binary packing model for FeSi/Fe powder mixture')
plt.savefig('FeSi Bi packing.png', bbox_inches='tight')
plt.show()
```